*J. Fluid Mech.* (1992), *vol.* 241, *pp.* 23–57
*Printed in Great Britain*

# Geostrophic adjustment in a channel: nonlinear and dispersive effects

By G. G. TOMASSON AND W. K. MELVILLE†
R. M. Parsons Laboratory, Massachusetts Institute of Technology, Cambridge,
MA 02139, USA

(Received 23 August 1991 and in revised form 17 December 1991)

We consider the general problem of geostrophic adjustment in a channel in the weakly nonlinear and dispersive (non-hydrostatic) limit. Governing equations of Boussinesq-type are derived, based on the assumption of weak nonlinear, dispersive and rotational effects, both for surface waves on a homogeneous fluid and internal waves in a two-layer system. Numerical solutions of the Boussinesq equations are presented, giving examples of the geostrophic adjustment in a channel for two different kinds of initial disturbances, both with non-zero perturbation potential vorticity. The timescales of rotational separation (that is, the separation of the Kelvin and Poincaré waves due to their dispersive properties) and that of nonlinear evolution are considered, with particular concern for the resonant interactions of nonlinear Kelvin waves and linear Poincaré waves described by Melville, Tomasson & Renouard (1989). A parameter measuring the ratio of the two timescales is used to predict when the free and forced Poincaré waves may be separated in the solution. It also distinguishes the cases in which the linear solutions are valid for the rotational separation from those requiring the full Boussinesq equations. Finally, solutions for the evolution of nonlinear internal waves in a sea strait are presented, and the effects of friction on the wavefront curvature of the nonlinear Kelvin waves are briefly considered.

## 1. Introduction

Gill (1976) considered the adjustment under gravity of an initial disturbance in a rotating channel, in the linear and hydrostatic limit. With these assumptions, the motion of a stratified fluid can be separated into normal modes, with the solution for each mode being equivalent to the solution for a homogeneous fluid with a free surface and a certain equivalent depth. He studied the problem of an initial discontinuity in the free surface of a homogeneous fluid, but his method applies to arbitrary initial disturbances as well. In the narrow channel limit, $W \ll R$, rotational effects are suppressed and the problem reduces to the non-rotating case, while for a very wide channel, $W \gg R$, it reduces to the well-known Rossby adjustment problem for an infinite ocean. The problem for a finite-width channel, $W = O(R)$, is solved by using the conservation of potential vorticity in the fluid, much like the Rossby adjustment problem. However, as stressed by Gill (1976), 'the sidewall boundaries in the finite width channel introduce some fundamentally new features, as the Kelvin

---

† Present address: Scripps Institution of Oceanography, University of California, San Diego, La Jolla CA 92093-0213, USA.

wave associated with each boundary only propagates in one direction, i.e. with the boundary on the right-hand side, when looking in the direction of propagation' (in the Northern hemisphere). The initial disturbance splits up into different left- and right-going disturbances, both made up of a leading Kelvin wave followed by a train of Poincaré waves, the Poincaré modes trailing due to their lower group speed. Behind the outgoing disturbances a boundary current is set up in the channel. The current follows the left-hand boundary (looking downstream) to the position of the initial discontinuity (the potential-vorticity front), then crosses the channel and continues downstream along the right-hand wall.

Gill's (1976) solutions are of importance for internal gravity wave motions in oceans and lakes, many of which evolve from the adjustment under gravity of localized initial disturbances. However, observations and field measurements indicate that nonlinear and dispersive (non-hydrostatic) effects may be important for many of these wave motions. Several authors, among them Ziegenbein (1969), Lacombe & Richez (1982), Armi & Farmer (1988), Farmer & Armi (1988) and La Violette & Arnone (1988), have presented visual observations and measurements of nonlinear internal wavetrains in the Strait of Gibraltar. Similar trains of internal waves have been measured by Gargett (1976) in the Strait of Georgia, BC, and by Farmer & Smith (1978) in Knight Inlet, BC. The waves in the Strait of Gibraltar are believed to evolve from an internal lee wave generated by the westward tidal flow over bottom topography in the western part of the Strait. As the tide slackens and eventually turns, the lee wave evolves into a train of nonlinear internal waves.

Pierini (1989) studied the evolution of the wave packet as it propagates eastward along the Strait and into the Alboran Sea. He solves a Kadomtsev–Petviashvili (KP) equation for a two-layer, inviscid fluid, and neglected rotational effects, although he noted that they can be important, especially inside the Strait, where the waves interact with the lateral boundaries. In fact, the measurements by Lacombe & Richez (1982) indicate that the eastward-propagating internal waves have a Kelvin wave structure, i.e. amplitude decaying away from the southern coast.

Similar trains of nonlinear internal waves have been observed in long and narrow thermally stratified lakes by Thorpe, Hall & Crofts (1972), Hunkins & Fliegel (1973) and Farmer (1978). However, the generation mechanism for these waves is quite different from that described above for the waves in the Strait of Gibraltar. Rather than being generated by tidal flow over bottom topography, their generation has typically been related to forcing by winds blowing along the axis of the lake, pushing the warmer water up against the end of the lake, generating a localized disturbance to the equilibrium stratification due to the excess of warm water. Again, rotational effects, which are expected to be important for these wave motions, are not included in most modelling efforts.

Maxworthy (1983) and Renouard, Chabert d'Hieres & Zhang (1987) conducted experiments on nonlinear and dispersive waves in a rotating channel, observing solitary-like Kelvin waves evolving from an initial disturbance in a stratified fluid. Most notably, the waves had wavecrests curving backwards away from the right-hand wall with their amplitude attenuating as they propagated along the channel. Grimshaw (1985) studied these wave motions theoretically, employing a KP equation modified to include rotational effects, but was not able to account for the wavefront curvature in the absence of viscous effects. Later, Katsis & Akylas (1987) solved the modified KP equation numerically and found their solutions to agree qualitatively with the experimental observations of wavefront curvature and amplitude attenuation along the channel. Melville, Tomasson & Renouard (1989) used a set of coupled evolution equations, which are asymptotically equivalent to the modified KP equation, and utilizing both numerical and approximate analytical solutions, explained the backward curvature and amplitude attenuation along the channel as being due to resonant interactions between the nonlinear Kelvin waves and linear Poincaré waves of the channel, with the former being unstable due to resonant forcing of the latter. However, as discussed in detail by Grimshaw & Melville (1989), the coupled evolution equations, as well as the modified KP equation, suffer from certain constraints on their initial data, and are therefore not valid as model equations for the geostrophic adjustment of *arbitrary* initial disturbances in a channel, but apply only to specific initial disturbances with zero perturbation potential vorticity.

Although he only considered the linear problem of geostrophic adjustment in a channel, Gill (1976) conjectured that it may only be the first stage in the adjustment process, the second stage being the nonlinear evolution on a slower timescale, with the associated advection of potential vorticity. Hermann, Rhines & Johnson (1989) studied the effects of nonlinear advection on the evolution of the potential vorticity front, noting that in the nonlinear problem the potential vorticity is conserved following the motion of the fluid elements. They consider the hydrostatic problem and assume that the linear adjustment (Gill's solution) is complete before the nonlinear adjustment begins, thus effectively taking the inertial timescale, $f^{-1}$, on which the linear adjustment takes place, to be much smaller than the timescale for nonlinear advection. They found that owing to the nonlinear advection of potential vorticity, the fluid eventually flows downchannel on both boundaries downstream of the initial potential vorticity front, rather than just on the right-hand side of the channel, as in the linear solution.

However, as noted above, both nonlinear and dispersive (non-hydrostatic) effects are believed to be important for many of the internal waves observed in oceans and lakes. Also, it is of interest to consider cases where the timescales of linear adjustment and nonlinear evolution are not as clearly separated as Hermann *et al.* (1989) assume. Indeed, from the linear dispersion curves of the channel, together with the dispersion curve for a nonlinear Kelvin wave travelling at a constant speed, shown in figure 1, it may be seen that for the nonlinear resonances to be possible at longitudinal wavenumbers within the range of interest, the timescales of rotational separation (that is, the separation of the linear Kelvin and Poincaré models due to their dispersive properties) and of nonlinear evolution are required to be of the same order of magnitude. This corresponds to weak rotational and nonlinear effects, and is indeed the appropriate scaling for many of the internal wave motions observed in oceans and lakes.

In this paper we consider the general problem of geostrophic adjustment of an arbitrary initial disturbance in a channel. In §2 a set of Boussinesq equations with weak nonlinear, dispersive and rotational effects, are derived for a homogeneous fluid. (In Appendix A the corresponding equations for internal waves in a two-layer system are derived.) These equations are more general than the KP equations and related evolution equations, and have no constraints on their initial data. A numerical scheme to solve these equations is introduced in §3, and described in more detail in Appendix B. In §4 we give examples of the nonlinear and dispersive geostrophic adjustment in a channel and compare them with the corresponding linear solutions. In §5 we consider the timescales of rotational separation and nonlinear evolution, introducing a parameter which measures the ratio of the two timescales. This permits us to predict the cases for which the linear solution is valid

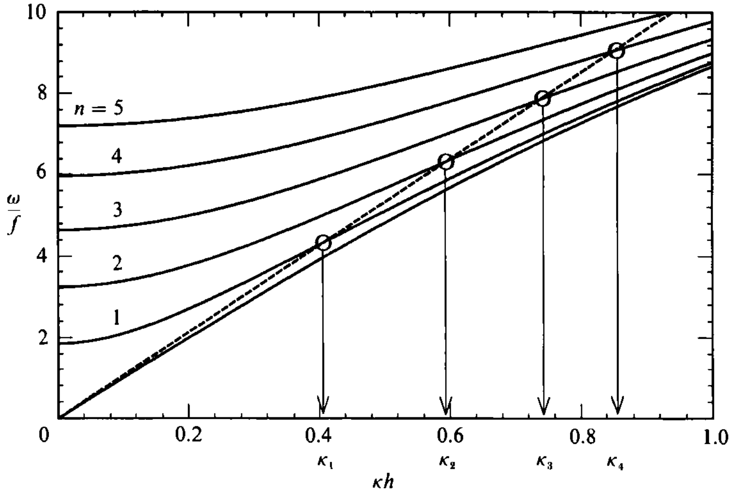

FIGURE 1. The dispersion curves for the linear modes of the channel (——) and the nonlinear Kelvin wave (---), showing the possibility of resonant interactions at the longitudinal wavenumbers $\kappa_1$, $\kappa_2$,.... Here $\omega$ is the radian frequency, $f$ is the Coriolis parameter and $h$ is a depth scale.

for the rotational separation, as well as predicting the cases for which the free and forced Poincaré waves may be separated in the solution. Finally, in §6, the results of the paper are discussed and applications of the numerical model to the internal waves in the Strait of Gibraltar are presented.

## 2. Formulation of the problem

Rather than studying the more complex two-layer problem for a stratified fluid, which is the appropriate formulation for most of the nonlinear and dispersive internal waves observed in ocean and lakes, we chose to look at the slightly simpler, but similar problem of surface waves on a homogeneous fluid in a rotating channel. The corresponding derivation for a two-layer fluid with a rigid lid is presented in Appendix A and applied by Renouard, Tomasson & Melville (1992) to comparisons with laboratory measurements. The details of both derivations are given by Tomasson (1991). Notwithstanding the slightly different equations, the important dynamics of the problem are the same in both cases.

### 2.1. *Derivation of Boussinesq equations*

We consider the motion of a homogeneous and inviscid fluid confined to a channel rotating on an $f$-plane, i.e. with constant Coriolis parameter. The $x$-axis is taken to be along the channel, the $y$-axis across the channel and the $z$-axis in the vertical direction, positive upwards. The channel has constant depth $h$ and width $W$, with a free surface with an equilibrium position at $z = 0$.

To derive equations with weak nonlinear, dispersive and rotational effects three small parameters are introduced:

$$\alpha = a/h, \tag{2.1}$$

$$\beta = (kh)^2, \tag{2.2}$$

$$\epsilon = (1/kR)(l/k), \tag{2.3}$$

representing weak nonlinear, dispersive and rotational effects, respectively. Here, $a$

is a typical wave amplitude, $k^{-1}$ and $l^{-1}$ are typical lengthscales in the $x$- and $y$-directions, respectively, and $R = c_0/f$ is the Rossby radius of deformation, where $c_0$ is the linear phase speed and $f$ is the Coriolis parameter. With the scaling

$$\left.\begin{aligned} x = k^{-1}x', \quad y = l^{-1}y', \quad z = hz', \\ u = \alpha c_0 u', \quad v = \alpha\gamma^{\frac{1}{2}}c_0 v', \quad w = \alpha\beta^{\frac{1}{2}}c_0 w', \\ t = (1/kc_0)t', \quad \eta = a\eta', \quad p = \alpha\rho c_0^2 p', \end{aligned}\right\} \tag{2.4}$$

where primes denote the non-dimensional variables, and assuming that

$$\alpha = O(\beta) \ll 1, \tag{2.5}$$

i.e. weak nonlinear and dispersive effects, the Euler equations become (dropping the primes for convenience)

$$u_x + \gamma v_y + w_z = 0, \tag{2.6}$$

$$u_t + \alpha u u_x + \alpha\gamma v u_y + \alpha w u_z - \epsilon v + p_x = 0, \tag{2.7}$$

$$\gamma v_t + \alpha\gamma u v_x + \alpha\gamma^2 v v_y + \alpha\gamma w v_z + \epsilon u + \gamma p_y = 0, \tag{2.8}$$

$$\beta w_t + p_z = O(\alpha\beta), \tag{2.9}$$

with the no-flux boundary condition at the bottom

$$w = 0 \quad \text{at} \quad z = -1, \tag{2.10}$$

the kinematic and dynamic boundary conditions at the surface

$$w = \eta_t + \alpha u \eta_x + \alpha\gamma v \eta_y \quad \text{at} \quad z = \alpha\eta, \tag{2.11}$$

$$p = \eta \quad \text{at} \quad z = \alpha\eta, \tag{2.12}$$

and the no-flux boundary conditions at the sidewalls of the channel

$$v = 0 \quad \text{at} \quad y = 0,\ W. \tag{2.13}$$

Here we have subtracted the hydrostatic pressure from the total pressure in the fluid, thus $p$ is the dynamic pressure only. $u$, $v$ and $w$ are the fluid velocities in the $x$-, $y$- and $z$-directions, respectively. The parameter

$$\gamma = l/k \tag{2.14}$$

measures the strength of transverse effects.

From (2.7)–(2.9), we see that to the lowest order in $\alpha$ and $\beta$, $u$, $v$ and $p$ must be independent of depth. This allows us to expand the solutions for these variables in the small parameter $\beta$:

$$[p, u, v](x, y, z, t) = [P, U, V](x, y, t) + \beta[\tilde{p}, \tilde{u}, \tilde{v}](x, y, z, t), \tag{2.15}$$

with the lowest order solution independent of $z$, i.e. hydrostatic. Using this in (2.6), integrating in $z$ and substituting into (2.9), using the boundary conditions (2.10) and (2.12) gives

$$p(x, y, z, t) = \eta(x, y, t) + \beta(U_{xt} + \gamma V_{yt})\,[\tfrac{1}{2}z^2 + z] + O(\beta^2). \tag{2.16}$$

Substituting (2.16) into the horizontal momentum equations (2.7) and (2.8) gives

$$U_t + \alpha U U_x + \alpha\gamma V U_y - \epsilon V + \eta_x + \beta\tilde{u}_t - \beta\epsilon\tilde{v} + \beta(U_{xxt} + \gamma V_{xyt})\,[\tfrac{1}{2}z^2 + z] = O(\beta^2), \tag{2.17}$$

$$\gamma V_t+\alpha\gamma UV_x+\alpha\gamma^2 VV_y+\epsilon U+\gamma\eta_y+\beta\gamma\tilde{v}_t+\beta\epsilon\tilde{u}+\beta\gamma(U_{xyt}+\gamma V_{yyt})\left[\tfrac{1}{2}z^2+z\right] = O(\beta^2). \tag{2.18}$$

Taking the lowest-order velocities, $U$ and $V$, to represent the depth-averaged velocities, we get, after averaging (2.17) and (2.18) over the depth of the fluid,

$$U_t+\alpha UU_x+\alpha\gamma VU_y-\epsilon V-\tfrac{1}{3}\beta(U_{xxt}+\gamma V_{xyt})+\eta_x = O(\beta^2), \tag{2.19}$$

$$\gamma V_t+\alpha\gamma UV_x+\alpha\gamma^2 VV_y+\epsilon U-\tfrac{1}{3}\beta\gamma(U_{xyt}+\gamma V_{yyt})+\gamma\eta_y = O(\beta^2). \tag{2.20}$$

To get a corresponding continuity equation, substitute (2.15) into the continuity equation (2.6) and integrate over the depth of the fluid, using the boundary conditions (2.10) and (2.11). This gives

$$U_x+\gamma V_y+\eta_t+\alpha[\eta U]_x+\alpha\gamma[\eta V]_y = O(\beta^2). \tag{2.21}$$

The equations (2.19)–(2.21) constitute a set of Boussinesq equations valid for all rotation rates. We now use the assumption of weak rotational effects

$$\epsilon = O(\alpha,\, \beta) \ll 1 \tag{2.22}$$

to rewrite the dispersive terms, using the lowest-order balances in the equations. This gives the Boussinesq equations

$$U_x+\gamma V_y+\eta_t+\alpha[\eta U]_x+\alpha\gamma[\eta V]_y = O(\beta^2), \tag{2.23}$$

$$U_t+\alpha UU_x+\alpha\gamma VU_y-\epsilon V-\tfrac{1}{3}\beta(U_{xxt}+\gamma U_{yyt})+\eta_x = O(\beta^2), \tag{2.24}$$

$$\gamma V_t+\alpha\gamma UV_x+\alpha\gamma^2 VV_y+\epsilon U-\tfrac{1}{3}\beta\gamma(V_{xxt}+\gamma V_{yyt})+\gamma\eta_y = O(\beta^2), \tag{2.25}$$

with the boundary conditions at the side walls

$$V = 0 \quad \text{at} \quad y = 0,\, W. \tag{2.26}$$

Here, (2.23) represents conservation of mass, while (2.24) and (2.25) represent conservation of momentum in the $x$- and $y$-directions, respectively.

### 2.2. *Properties of the equations*

By assuming the solutions to be locally confined in space, i.e.

$$\lim_{x\to\pm\infty} (\eta, U, V) = 0, \tag{2.27}$$

or confined to a finite length channel, i.e.

$$U = 0 \quad \text{at} \quad x = 0,\, L, \tag{2.28}$$

the Boussinesq equations may be shown to exactly conserve mass, defined by

$$M = \int_0^L \int_0^W \eta(x,y,t)\,\mathrm{d}x\,\mathrm{d}y, \tag{2.29}$$

and to conserve the total energy of the solution, defined by

$$E = \frac{1}{2}\int_0^L \int_0^W \left[U^2+\gamma V^2+\eta^2+\tfrac{1}{3}\beta(U_x^2+\gamma U_y^2+\gamma V_x^2+\gamma^2 V_y^2)-\tfrac{1}{3}\alpha\eta^3\right]\mathrm{d}x\,\mathrm{d}y, \tag{2.30}$$

to second order in the small parameters. Here, the limits in $x$ are either $\pm\infty$, corresponding to (2.27), or (0, $L$), corresponding to (2.28). The expression for the energy consists of the lowest-order kinetic and potential energy, together with dispersive and nonlinear corrections.

The Boussinesq equations may also be shown to conserve potential vorticity, defined by

$$Q = \frac{\epsilon + \left[1 - \tfrac{1}{3}\beta\left(\dfrac{\partial^2}{\partial x^2} + \gamma \dfrac{\partial^2}{\partial y^2}\right)\right](\alpha\zeta)}{1 + \alpha\eta}, \tag{2.31}$$

to third order in the small parameters. Here, the second-order derivative terms represent a dispersive correction to the lowest-order relative vorticity

$$\zeta = \gamma(V_x - U_y). \tag{2.32}$$

### 2.3. *Evolution equations*

By considering waves moving in one direction only, a simpler set of coupled evolution equations used by Melville *et al.* (1989) and Tomasson & Melville (1990),

$$\eta_t + \eta_x + \tfrac{3}{2}\eta\eta_x - \tfrac{1}{6}\beta\eta_{xxt} + \tfrac{1}{2}\gamma V_y - \tfrac{1}{2}\epsilon V = O(\beta^2), \tag{2.33}$$

$$\gamma V_t + \epsilon\eta + \gamma\eta_y = O(\beta^2), \tag{2.34}$$

may be derived, as well as the asymptotically equivalent modified KP equation (Grimshaw & Melville 1989). However, as discussed in § 1, the evolution equations are not valid as model equations for arbitrary initial disturbances, but are constrained to initial disturbances with zero perturbation potential vorticity, thus limiting their applicability considerably. In this paper we will therefore solve the more general Boussinesq equations. Solutions of the Boussinesq equations with Kelvin-like initial disturbances satisfying the constraint of zero perturbation potential vorticity gave results very similar to the corresponding solutions of the evolution equations reported by Melville *et al.* (1989).

## 3. Numerical scheme

Before solving the Boussinesq equations (2.23)–(2.25) numerically, we rescale them, taking $a = h$, $k^{-1} = h$ and $l^{-1} = R$ in (2.4). This gives the equations

$$\eta_t + [(1+\eta)\,U]_x + \Gamma[(1+\eta)\,V]_y = 0, \tag{3.1}$$

$$U_t + \eta_x + UU_x + \Gamma VU_y - \Gamma V - \tfrac{1}{3}[U_{xxt} + \Gamma U_{yyt}] = 0, \tag{3.2}$$

$$V_t + \eta_y + UV_x + \Gamma VV_y + U - \tfrac{1}{3}[V_{xxt} + \Gamma V_{yyt}] = 0, \tag{3.3}$$

with the boundary conditions

$$V = 0 \quad \text{at} \quad y = 0,\ W. \tag{3.4}$$

Here

$$\Gamma = (h/R)^2, \tag{3.5}$$

and we have neglected the smaller-order terms on the right-hand side.

The above equations are solved numerically using a line-by-line iteration scheme developed and described in detail by Pedersen & Rygg (1987), Pedersen (1988) and

Rygg (1988). They developed the scheme for the equations without rotation, but we have extended it to include the rotational terms. The numerical scheme, which is described in Appendix B, was found to conserve mass and energy to within 0.5% accuracy for typical values of the gridspacings and timestep. It was also tested against analytical solutions of the linear, non-dispersive problem of geostrophic adjustment in a channel (see Gill 1976; Tomasson 1991), and for the propagation of the exact solitary wave solutions in the non-rotating problem. Both cases showed excellent agreement with the analytical solutions with the error in $\eta$ being less than 0.5%.

## 4. Examples of geostrophic adjustment in a channel

To study the geostrophic adjustment of an arbitrary initial disturbance in a channel we solve the Boussinesq equations (3.1)–(3.3) numerically using the scheme described above. In what follows, two examples will be given. In both cases the initial disturbance has non-zero perturbation potential vorticity, rendering the coupled evolution equations employed by Melville *et al.* (1989) and others inappropriate as model equations. Note that an infinitely long channel is simulated by ensuring that no disturbance reaches the endwalls of the channel in the numerical solutions.

The first example corresponds to an initial localized elevation of the surface whereas the second has an initial discontinuity in the surface, with the fluid at different levels on each side. Gill (1976) considered this second example in the linear and hydrostatic limit. In both cases the initial disturbance has no transverse variations and no associated flow velocities. An important factor that distinguishes these two cases is the amount of potential energy available from the initial disturbance, it being finite for the first case but infinite for the second. The two cases will be referred to as the 'step of finite length' and the 'step of semi-infinite length'.

### 4.1. *Step of finite length*

The first initial disturbance with non-zero perturbation potential vorticity we consider is a localized elevation of the surface, with no transverse variation and no associated flow velocities:

$$\eta(x,y,0) = \tfrac{1}{2}a\left\{1 \pm \tanh\left[\frac{x-(x_0 \mp \frac{1}{2}l)}{l_s}\right]\right\}, \tag{4.1}$$

$$U(x,y,0) = 0, \tag{4.2}$$

$$V(x,y,0) = 0, \tag{4.3}$$

i.e. a rectangularly shaped disturbance with the edges smoothed out by a tanh-function. The upper sign is taken for $x < x_0$ and the lower sign for $x > x_0$. The length of the disturbance is $l$ with its centre at $x = x_0$, $a$ is the amplitude of the disturbance and $l_s$ is a lengthscale of the smoothing functions, with $l_s$ typically much less than $l$. The initial disturbance is given in figure 2. Note that the potential energy associated with this initial disturbance is finite.

Here we present results for one set of parameters:

$$W/R = 2.0, \quad \Gamma = (h/R)^2 = 0.01, \quad a = 0.15, \quad x_0 = 0, \quad l = 20.0, \quad l_s = 2.0, \tag{4.4}$$

for both the linear problem, obtained by solving the linearized Boussinesq equations,

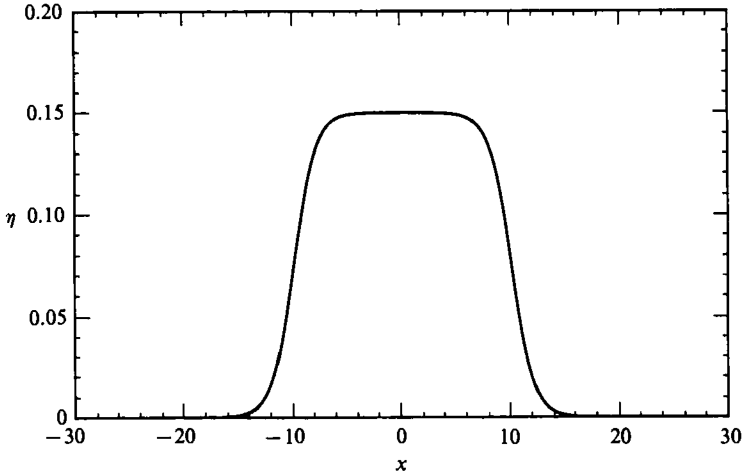

FIGURE 2. The initial disturbance to the surface used in the run for a step of finite length.

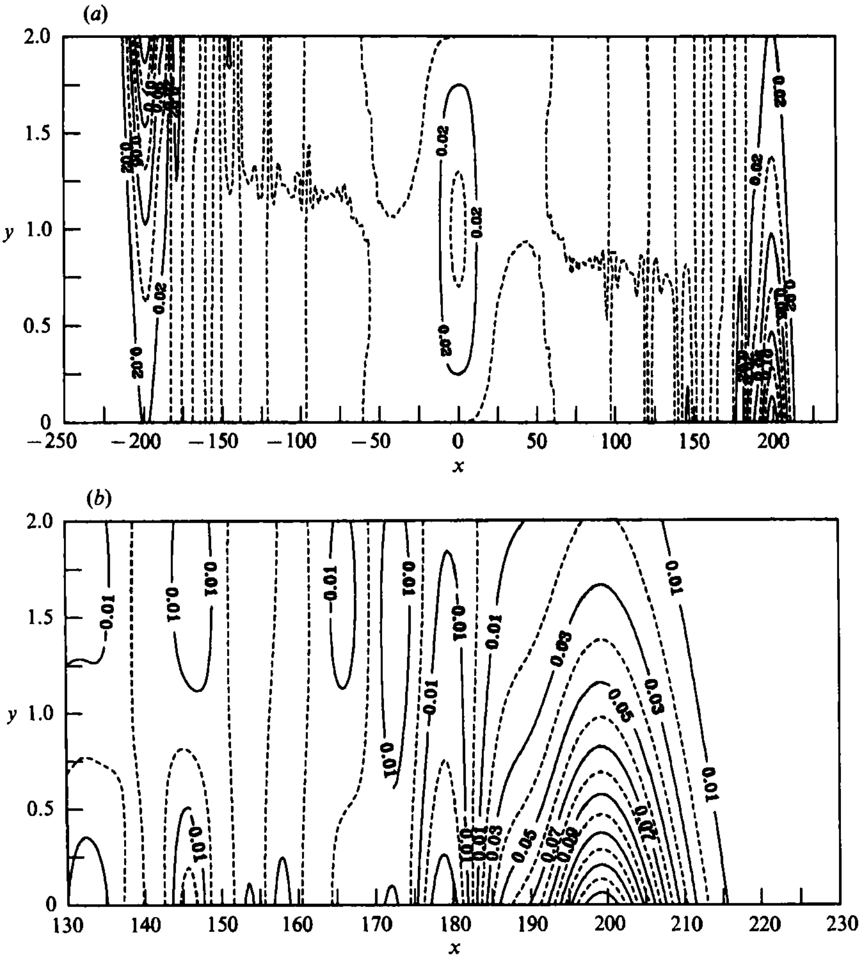

FIGURE 3. Contour plots of the solution of linearized versions of (3.1)–(3.3) for $\eta$ at $t = 200$ for the finite length step. (*a*) The solution over the whole channel. (*b*) The leading disturbance moving to the right.

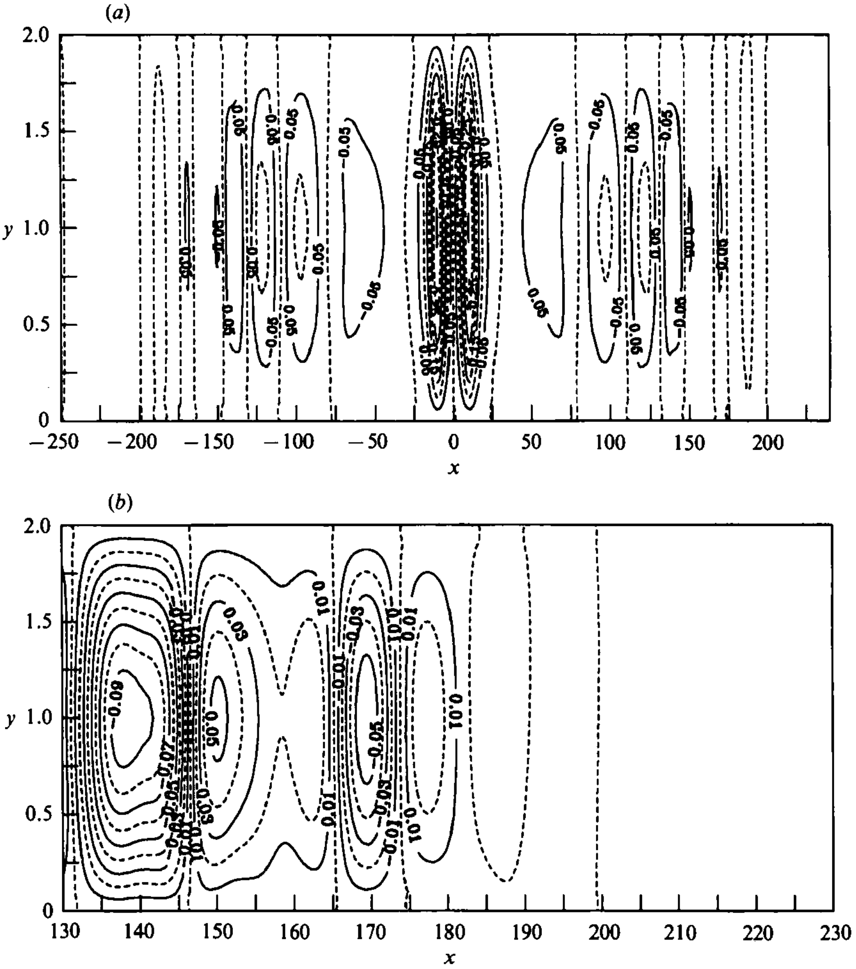

FIGURE 4. Contour plots of the solution of linearized versions of (3.1)–(3.3) for $V$ at $t = 200$ for the finite length step. (a) The solution over the whole channel. (b) The leading disturbance moving to the right.

and the corresponding nonlinear problem, obtained by solving the full Boussinesq equations. Note, that for both cases dispersive effects are included.

In figures 3 and 4 contour plots of the linear solution for $\eta$ and $V$ at $t = 200$ are given, both for the whole channel and a more detailed plot of the leading disturbance moving to the right. Figures 5 and 6 show the corresponding linear solutions. The disturbance splits up into a left- and a right-going disturbance, the two being identical (except for a reflection around the centreline of the channel), owing to the symmetry of the initial disturbance. The two disturbances are made up of leading Kelvin modes, followed by Poincaré modes, as can be seen quite clearly in the solution for $V$, recalling that no transverse velocity is associated with the Kelvin modes, and thus the solution for $V$ is made up of Poincaré modes only. The nonlinear evolution is evident in the solution for $\eta$ by the appearance of nonlinear Kelvin waves at the leading edge of the disturbance, with the associated wavefront curvature, and in the solution for $V$ by the appearance of high-frequency, resonantly generated Poincaré waves at the leading edge of the disturbance. At the location of the initial

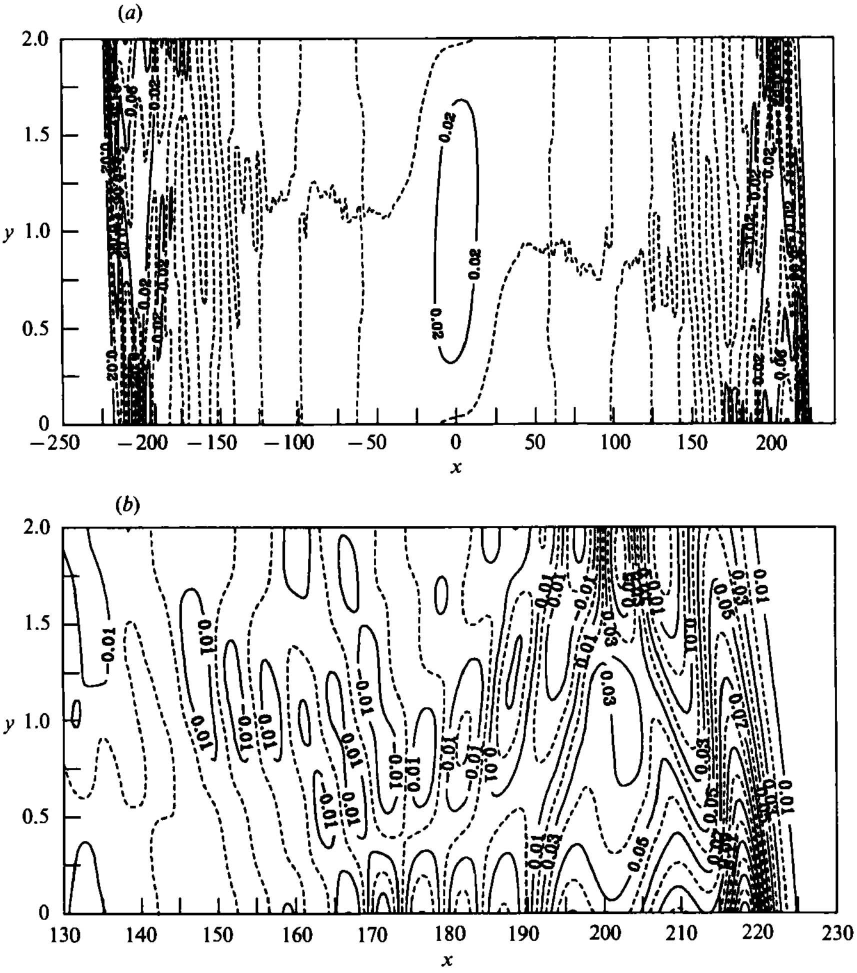

FIGURE 5. Contour plots of the nonlinear solution of (3.1)–(3.3) for $\eta$ at $t = 200$ for the finite length step. (*a*) The solution over the whole channel. (*b*) The leading disturbance moving to the right.

disturbance, where the perturbation potential vorticity is non-zero, a geostrophic eddy is set up, with the flow rotating clockwise in the channel and with an associated disturbance of the surface.

In figure 7 the amplitude of the leading wave is shown against distance down the channel for both linear and nonlinear cases. (Values are not available for the smallest times because the leading crest is not well defined at the initial stages of the evolution.) The effects of nonlinearities are evident, leading to higher amplitudes and an attenuation (although very weak) of the amplitude as the wave propagates down the channel. In figure 8 the spectra of the first five transverse modes of $V$ (Poincaré modes) are plotted at $t = 200$ for both cases. Again, the effects of nonlinearity are evident from the peaks in the spectra of the nonlinear solution, associated with the direct resonant forcing of the Poincaré modes by the nonlinear Kelvin waves, as described by Melville *et al.* (1989), and explained in figure 1.

The ratio of the total energy retained by the geostrophic eddy versus that radiated away by the Kelvin and Poincaré waves was found to be the same (to our numerical accuracy) in the linear and nonlinear solutions.

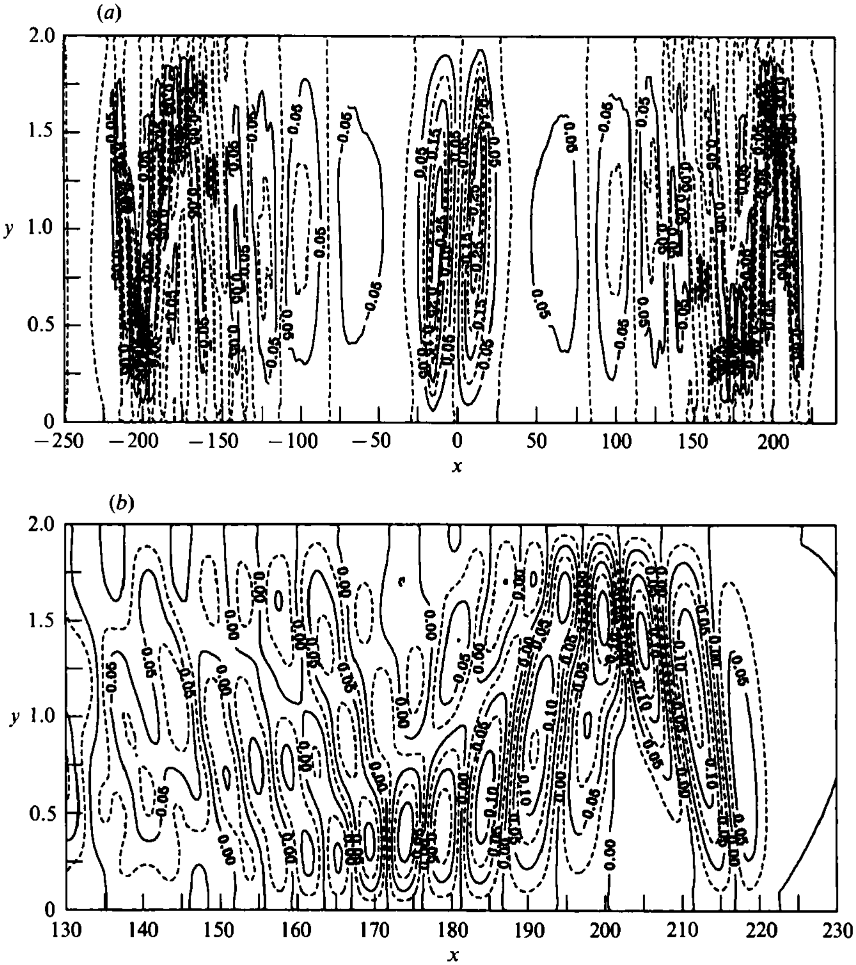

FIGURE 6. Contour plots of the nonlinear solution of (3.1)–(3.3) for $V$ at $t = 200$ for the finite length step. (a) The solution over the whole channel. (b) The leading disturbance moving to the right.

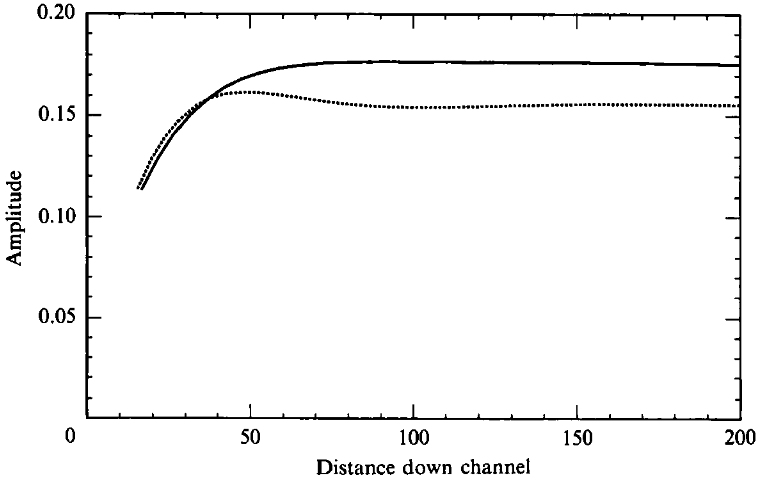

FIGURE 7. The amplitude of the leading wave moving to the right *vs.* distance down the channel for the step of finite length: ——, nonlinear; · · · · · ·, linear.

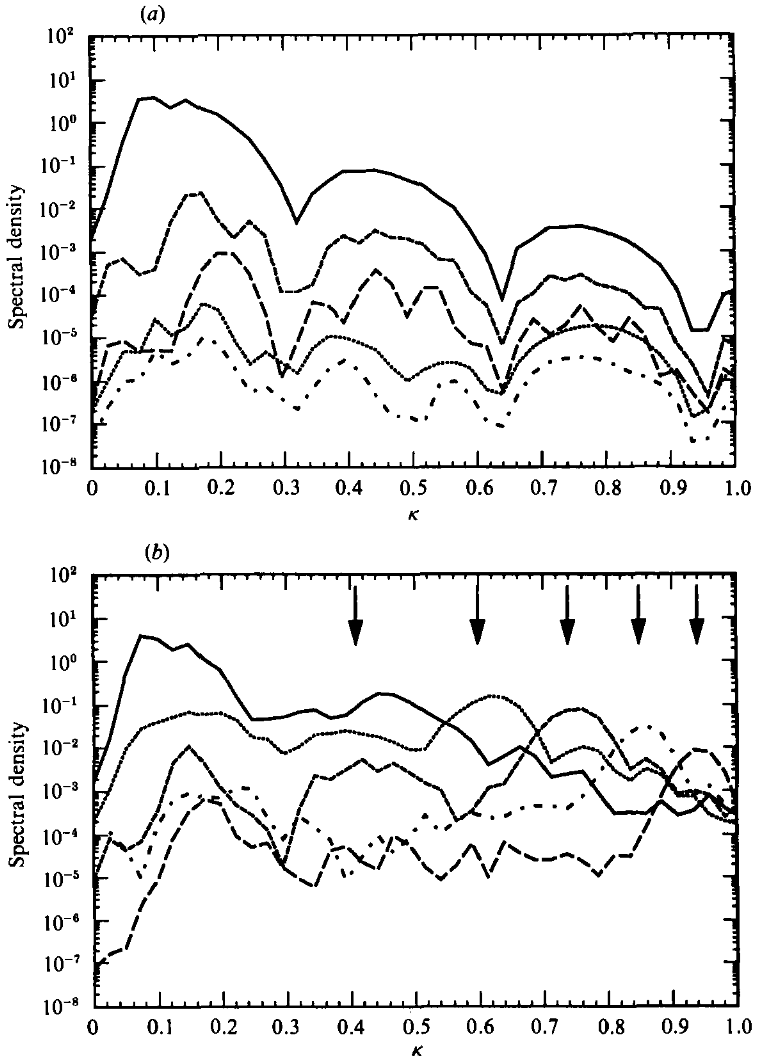

FIGURE 8. The spectra of the first five transverse modes of $V$ (Poincaré models) at $t = 200$ for the step of finite length. (*a*) The linear solution, (*b*) the nonlinear solution. The arrows indicate the wavenumbers of the direct nonlinear resonances, as predicted from the measured speed of the leading nonlinear Kelvin wave and the linear dispersion relationship (see Melville *et al.* 1989, and figure 1). ——, $n = 1$; · · · · ·, $n = 2$; - - - - - -; $n = 3$; —·—·—, $n = 4$; — — —, $n = 5$.

### 4.2. *Step of semi-infinite length*

The second kind of initial disturbance with non-zero perturbation potential vorticity we consider is a smooth change in the elevation of the surface with no associated flow velocities and no transverse variation, i.e.

$$\eta(x,y,0) = -a\tanh\left(\frac{x-x_0}{l_s}\right), \tag{4.5}$$

$$U(x,y,0) = 0, \tag{4.6}$$

$$V(x,y,0) = 0. \tag{4.7}$$

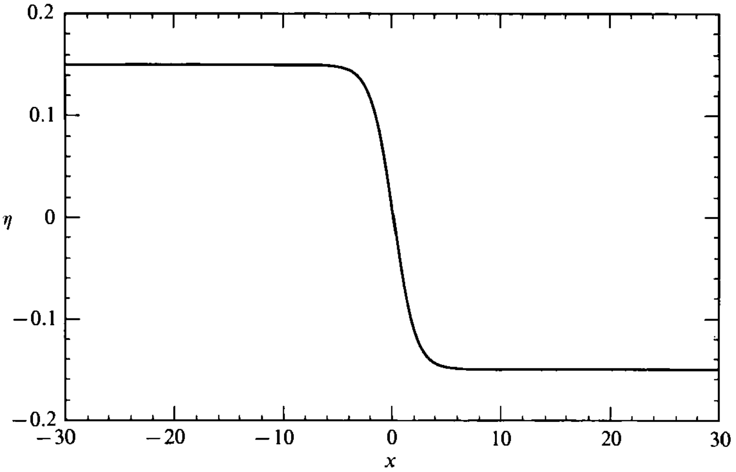

FIGURE 9. The initial disturbance to the surface used in the step of semi-infinite length.

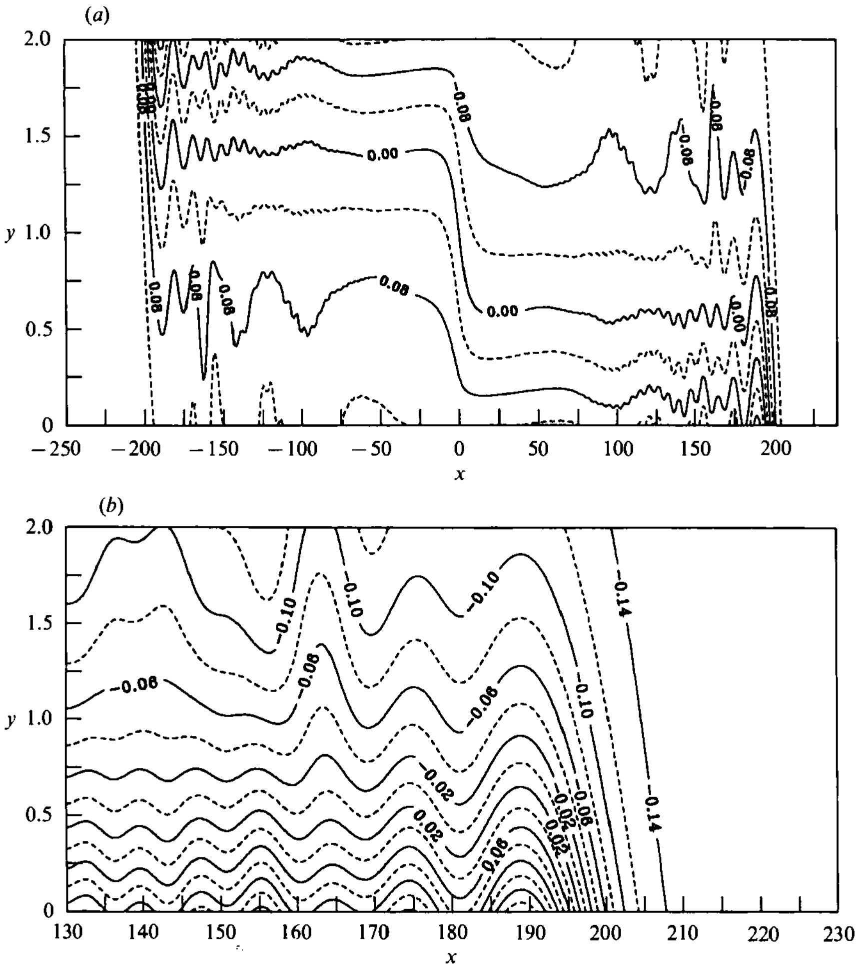

FIGURE 10. Contour plots of the solution of linearized versions of (3.1)–(3.3) for $\eta$ at $t = 200$ for the step of semi-infinite length. (a) The solution over the whole channel. (b) The leading disturbance moving to the right.

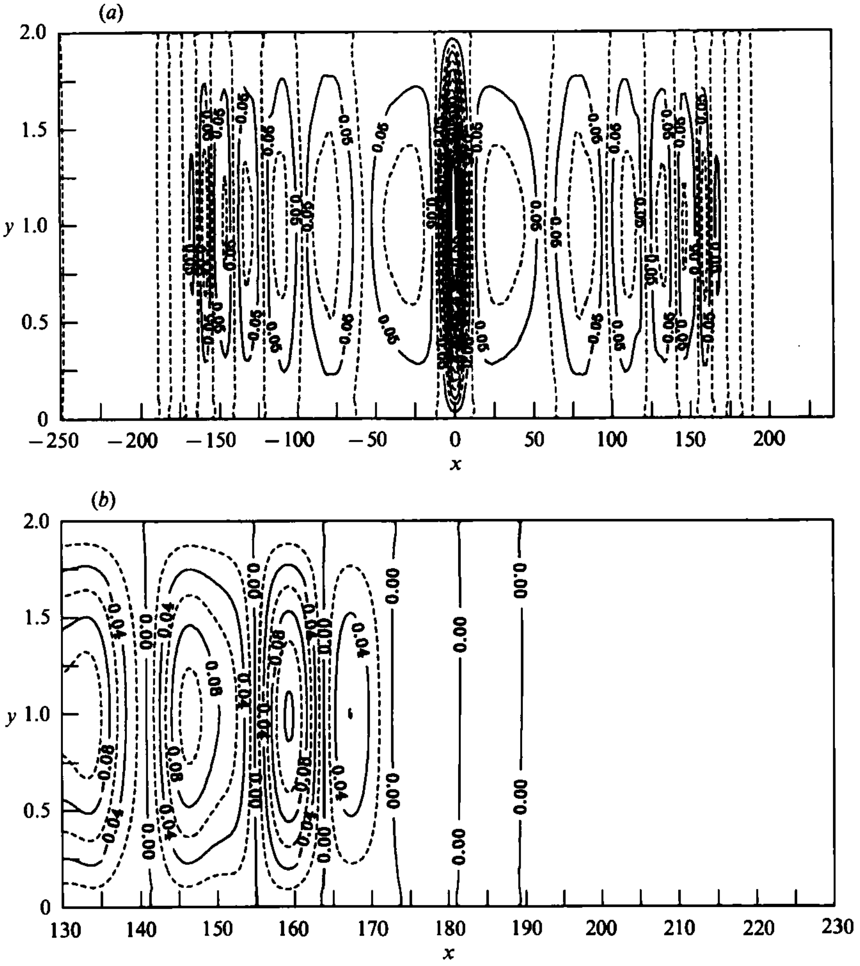

FIGURE 11. Contour plots of the solution of linearized versions of (3.1)–(3.3) for $V$ at $t = 200$ for the step of semi-infinite length. (*a*) The solution over the whole channel. (*b*) The leading disturbance moving to the right.

Here, $a$ is the amplitude of the discontinuity, $x = x_0$ is its location and $l_s$ is the lengthscale of the smoothing function. The initial disturbance is shown in figure 9. This problem corresponds to a dam with still water on both sides that breaks instantaneously at $t = 0$. Gill (1976) considered the same problem in the linear and hydrostatic limit, except for the smoothing of the discontinuity, which is necessary here for the resolution of the numerical scheme. Here, the potential energy available from the initial disturbance is infinite (infinitely long channel). Again, we present results for one set of parameters only, but for both the linear and the corresponding nonlinear problems, with dispersive effects included in both cases. The parameters $W/R$, $\Gamma$, $a$, $x_0$ and $l_s$ are the same as those given in (4.4).

In some respects this case is quite different from the one discussed in §4.1. Here, as discussed above, the potential energy associated with the initial disturbance is unlimited, whereas for the other case it is finite. Secondly, unlike the step of finite length, the initial disturbance considered here is not symmetrical with respect to the left and right parts of the channel, but rather is antisymmetrical. Thus, the

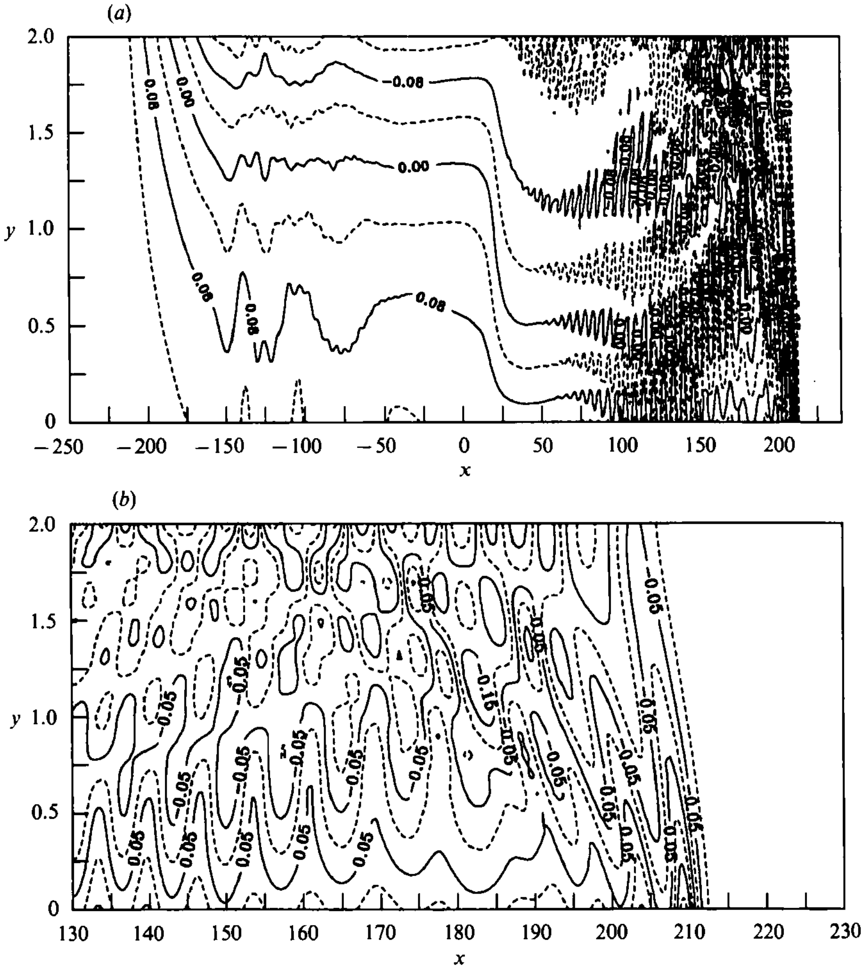

FIGURE 12. Contour plots of the nonlinear solution of (3.1)–(3.3) for $\eta$ at $t = 200$ for the step of semi-infinite length. (a) The solution over the whole channel. (b) The leading disturbance moving to the right.

disturbances propagating to the left and right in the channel will have different signs, the one propagating to the left will be negative, whereas the one propagating to the right will be positive. This has no significance for the linear problem, but in the nonlinear problem the effects of this difference are profound, as only positive disturbances may evolve into solitary waves.

Figures 10–15 correspond to those presented in §4.1. Figures 10–13 show contour plots of the linear and nonlinear solutions for $\eta$ and $V$ at $t = 200$, again giving the solution for the whole channel as well as a detailed plot of the leading disturbance moving to the right. The solution shows a Kelvin front moving in both directions, followed by a tail of Poincaré waves. Behind the fronts a boundary current is set up in the channel, flowing from left to right. To the left of the discontinuity in the potential vorticity the current is trapped against the left-hand wall (when looking in the direction of the flow), but crosses over the channel at the location of the discontinuity and flows along the right-hand wall to the right of it. In the linear problem, the left- and right-going disturbances are identical, except for a reflection

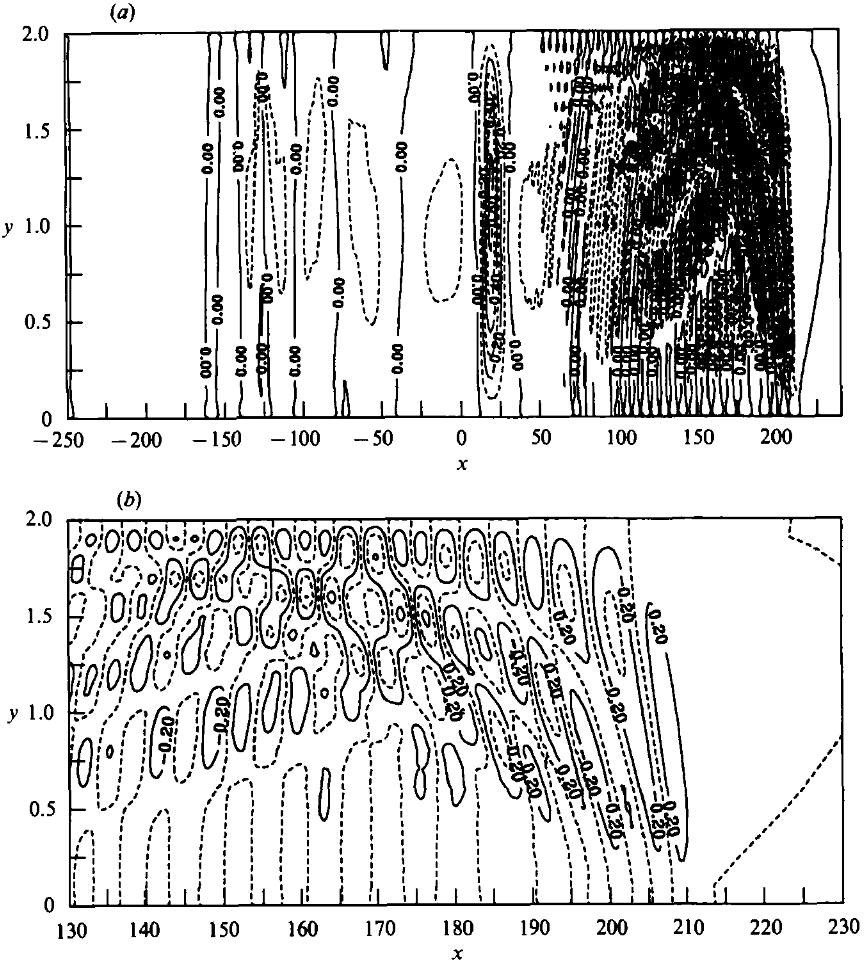

FIGURE 13. Contour plots of the nonlinear solution of (3.1)–(3.3) for $V$ at $t = 200$ for the step of semi-infinite length. (*a*) The solution over the whole channel. (*b*) The leading disturbance moving to the right.

around the centre of the channel and the sign of the disturbance. However, the nonlinear solution displays profound differences between the left- and right-going disturbances, in accordance with the discussion above. The right-going disturbance evolves into non-linear Kelvin waves with wavecrests curving backwards, and nonlinear and dispersive effects tending to balance one another, as seen above. However in the disturbance moving to the left the nonlinear and dispersive effects are not balanced and it evolves into a nonlinear and dispersive wavetrain due to its negative amplitude.

The amplitude of the leading wave moving to the right is shown in figure 14. The nonlinear effects lead to larger amplitudes, with the amplitude fluctuating rather than attenuating as the wave moves down the channel. Another interesting feature of the disturbance moving to the right is the apparently much richer structure in the tail of the leading wave, when compared with that from the step of finite length. This is also seen quite clearly in the spectra of the transverse modes of $V$ (Poincaré modes), given in figure 15 at $t = 200$ for both the linear and nonlinear cases. Rather than

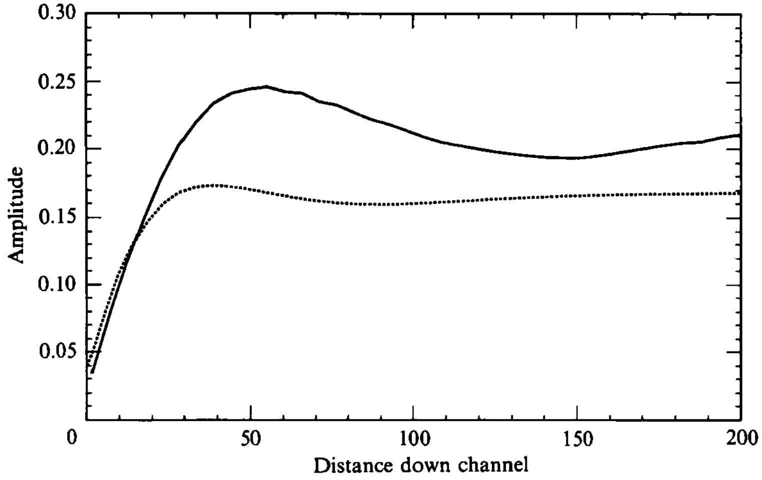

FIGURE 14. The amplitude of the leading wave moving to the right *vs.* distance down the channel for the step of semi-infinite length: ——, nonlinear; · · · · ·, linear.

seeing the peaks in the spectra of the Poincaré modes decreasing significantly in strength with increasing mode number, as was the case for the step of finite length, the peaks here are about the same strength for the first five modes shown in the figure, and in fact were found to be about the same strength all the way up to mode nine or ten. Also, the peaks are not as well tuned into the resonant wavenumbers, with some of the modes displaying double peaks around the resonant wavenumber. The reason for this difference may be the stronger forcing due to the unlimited source of potential energy, or the appearance of more than one nonlinear Kelvin wave, travelling at slightly different speeds.

## 5. Timescales of rotational separation and nonlinear evolution

In §§1 and 2 we discussed how the coupled evolution equations may be employed as model equations for the evolution of an initial disturbance in a channel if the associated perturbation potential vorticity is zero. The simplest way to satisfy this requirement is for the transverse structure to be that of a linear Kelvin wave, i.e. exponentially decaying in the transverse direction, with the transverse velocity vanishing identically, as was done by Melville *et al.* (1989). Also, owing to the properties of the linear dispersion relationships, the Kelvin modes have greater group speeds than the Poincaré modes. Thus, as the disturbance evolves in time, the Kelvin modes will lead the Poincaré mode transients and eventually separate from them in space. However, these transient Poincaré waves may not be the only ones present in the solution. In Melville *et al.* (1989) and in §4 we have seen how the nonlinear Kelvin waves may generate Poincaré waves through nonlinear resonances. Consequently, we may see Poincaré waves of two different origins in the solution, the transients evolving from the initial disturbance and the resonantly generated waves.

In view of the above, it is of interest to test Gill's conjecture by comparing the timescale of rotational separation, i.e. the separation of the Kelvin and Poincaré modes, and the timescale of the nonlinear evolution. For those situations where the rotational separation takes place before nonlinear effects become important, the Poincaré waves of different origins can be separated. Also, these cases may be modelled by first solving the linear problem for the initial evolution, using Gill's

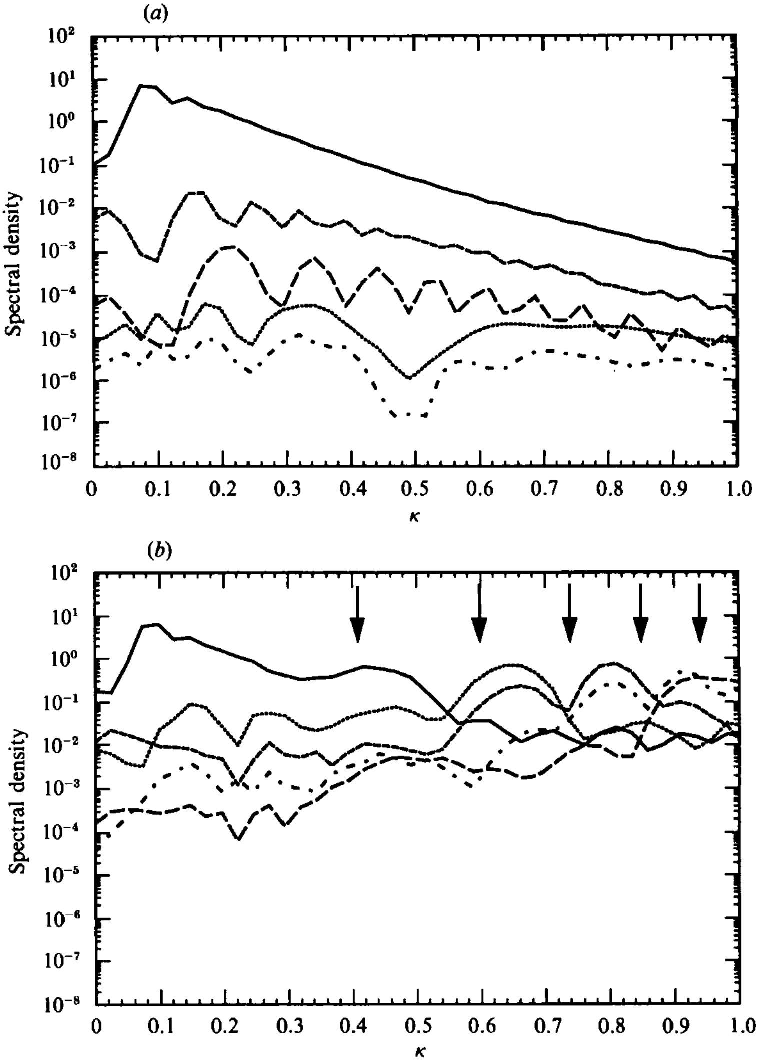

FIGURE 15. The spectra of the first five transverse modes of $V$ (Poincaré modes) at $t = 200$ for the step of semi-infinite length. (*a*) The linear solution, (*b*) the nonlinear solution. The arrows indicate the wavenumbers of the direct resonances, as predicted from the measured speed of the nonlinear leading Kelvin wave and the linear dispersion relationship (see Melville *et al.* 1989, and figure 1). ——, $n = 1$; · · · · · ·, $n = 2$; ------, $n = 3$; —·—·—, $n = 4$; ———, $n = 5$.

(1976) classical analytical solution, and subsequently solving the coupled evolution equations for the nonlinear evolution of leading Kelvin wave disturbance. Otherwise, the Poincaré waves of different origin cannot be separated.

The simplest way to obtain a quantitative measure of these two effects is to directly compare their timescales. The timescale for rotational separation, $T_R$, is given by (see Appendix C for details of the derivation)

$$T_R = O(kR)^2, \tag{5.1}$$

where we have assumed $W/R = O(1)$. The timescale for nonlinear effects, $T_N$, is given by

$$T_N = O(1/\alpha). \tag{5.2}$$

| Run | $W/h$ | $W/r$ | $a_0/h$ | $\Pi$ |
|---|---|---|---|---|
| I | 10 | 1.0 | 0.01 | 0.1 |
| II | 10 | 1.0 | 0.1 | 1.0 |
| III | 10 | 4.0 | 0.01 | 0.006 |
| IV | 10 | 4.0 | 0.1 | 0.06 |
| V | 40 | 1.0 | 0.01 | 1.6 |
| VI | 40 | 1.0 | 0.1 | 16 |

TABLE 1. The parameters used in the runs for the timescales of rotational separation and nonlinear evolution.

The ratio of the two timescales, $\Pi$, is given by

$$\Pi = \alpha(kR)^2. \tag{5.3}$$

(This parameter is similar to the Ursell number, which measures the ratio of the timescales of nonlinear and dispersive effects.) Note that although we refer to the separation as being due to rotation alone, it is also due to three-dimensional effects, measured by $W$ instead of $R$ (see Appendix C). In fact, the smaller of $W$ and $R$ will be the dominant one in the expression for the timescale of separation (replacing $R$ in (5.1)). Although (5.1) is formally valid for $W/R = O(1)$, the magnitude of the parameter is very sensitive to changes in $W$ and $R$ owing to the second power involved. Therefore, in all the results presented here, $R$ is taken to be smaller than or equal to $W$ to ensure that (5.1) is a true estimate of the timescale of separation. Also note that the assumption of weak rotation in the derivation of the Boussinesq equations, together with the assumption of weak nonlinear effects, give $\Pi \geqslant O(1)$. However, the assumption of weak rotation was only necessary to rewrite the highest-order, dispersive terms in the equations. The rotational and nonlinear terms are not affected by this assumption, and those terms in the equations are valid for strong rotation as well. This justifies looking at cases with $\Pi < O(1)$ as well as $\Pi \geqslant O(1)$.

The magnitude of the parameter $\Pi$ leads to the following interpretations:

$\Pi \ll 1$: $T_R$ is much smaller than $T_N$ with the Kelvin waves separating from the Poincaré waves before nonlinear effects become important.

$\Pi \gg 1$: $T_R$ is much larger than $T_N$ with the nonlinear evolution taking place before the Kelvin waves separate from the Poincaré waves. The resonantly generated Poincaré waves cannot be separated from the transient Poincaré waves.

$\Pi = O(1)$: the two timescales are comparable and the nonlinear evolution and rotational separation take place simultaneously. The resonantly generated Poincaré waves cannot be clearly separated from the transient Poincaré waves,

In the following we will give several examples of solutions with different values of $\Pi$. In all of these examples the initial disturbance is a step of finite length like that used in §4.1, but with different amplitudes. The lengthscale, $k^{-1}$ in (5.3), is taken to correspond to the first zero crossing in the spectra of the initial disturbance, i.e.

$$k^{-1} = l/\pi, \tag{5.4}$$

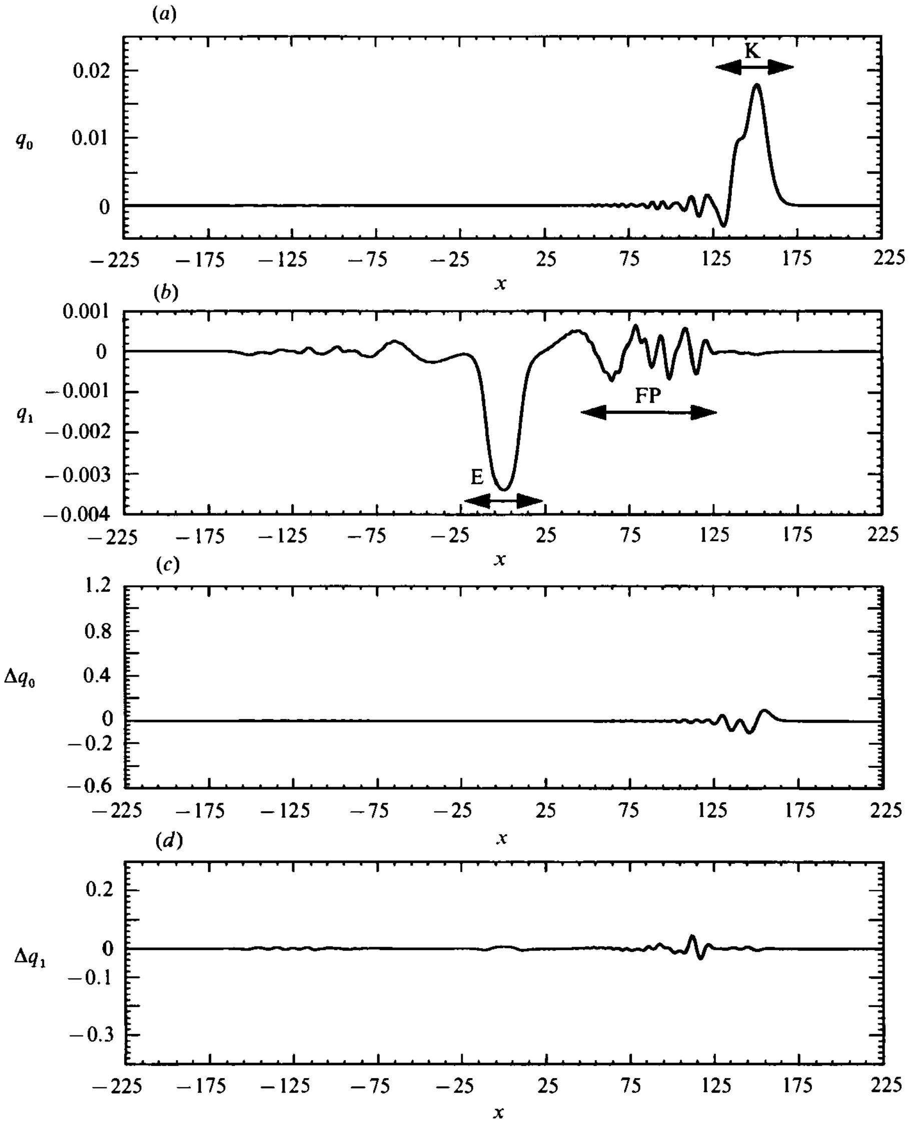

FIGURE 16. Run I ($\Pi = 0.1$) at $t = 150$. (*a*) The Kelvin mode, (*b*) the first Poincaré mode, (*c*) the difference between the nonlinear and linear solution for the Kelvin mode, (*d*) the difference between the nonlinear and linear solution for the first Poincaré mode. K, E, FP and RP indicate the approximate regimes of the leading Kelvin wave, the geostrophic eddy and the free and resonantly forced Poincaré waves, respectively.

where $l$ is the length of the disturbance. This choice is sufficiently accurate as the expressions for the timescales are order of magnitude only.

To quantify the rotational separation we introduce the new variables

$$q = \eta + U, \tag{5.5}$$

$$r = \eta - U. \tag{5.6}$$

These variables were used by Gill (1982) in the analytical solution to the linear, hydrostatic problem. Their advantage is that the Kelvin waves moving to the left and right are separated with $q$ containing only the Kelvin wave moving to the right

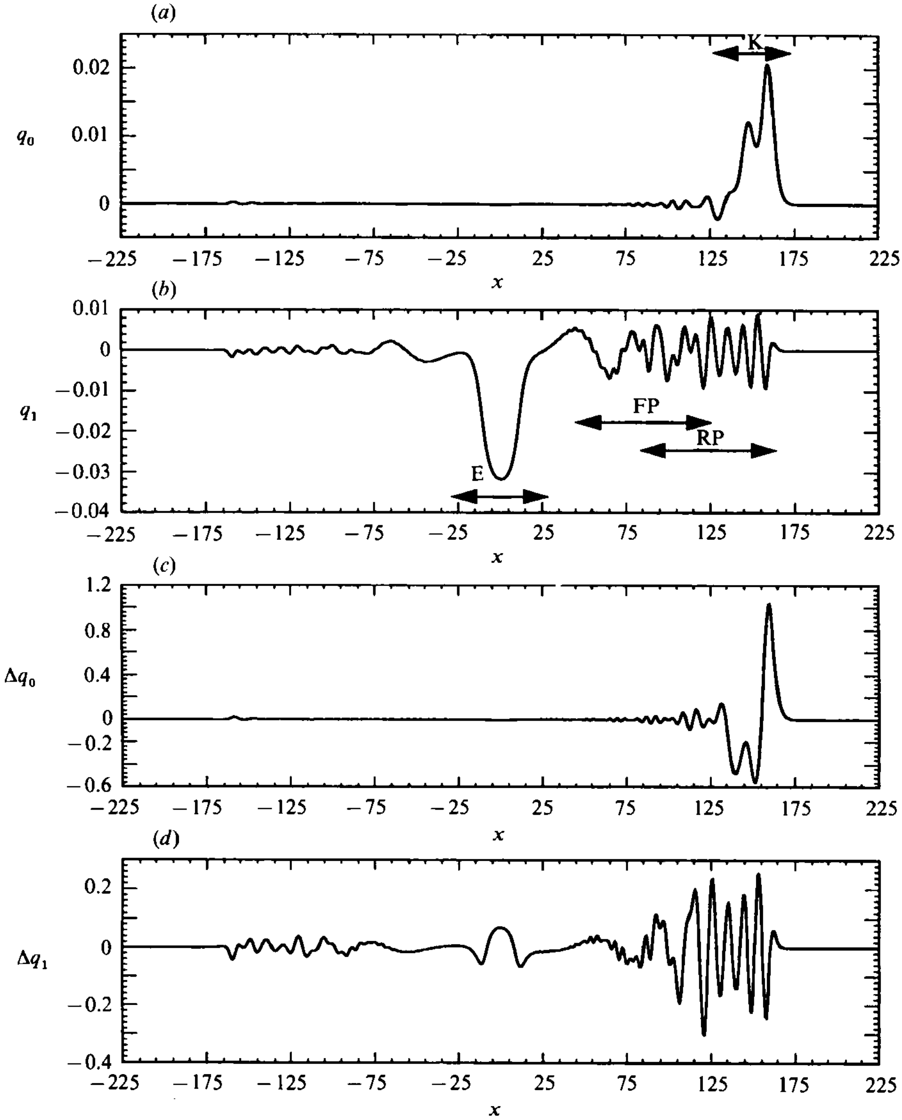

FIGURE 17. As in figure 16, except $\Pi = 1.0$ (Run II).

and $r$ containing only the Kelvin wave moving to the left. Although the above only holds for the linear, hydrostatic case, the variables are useful here as well, owing to the weakness of the nonlinear and dispersive effects. The variables can be expanded in the transverse direction into a set comprised of a Kelvin mode and Poincaré modes:

$$q(x,y,t) = q_0(x,t)\,\mathrm{e}^{-y} + \sum_{n=1}^{\infty} q_n(x,t)\left[\cos\frac{n\pi y}{W} - \frac{W}{n\pi}\sin\frac{n\pi y}{W}\right], \tag{5.7}$$

$$r(x,y,t) = r_0(x,t)\,\mathrm{e}^{+y} + \sum_{n=1}^{\infty} r_n(x,t)\left[\cos\frac{n\pi y}{W} + \frac{W}{n\pi}\sin\frac{n\pi y}{W}\right], \tag{5.8}$$

where the zero mode is the Kelvin mode and $n = 1, 2, \ldots$ are the Poincaré modes. These transverse modal functions form a complete and an orthogonal set and may

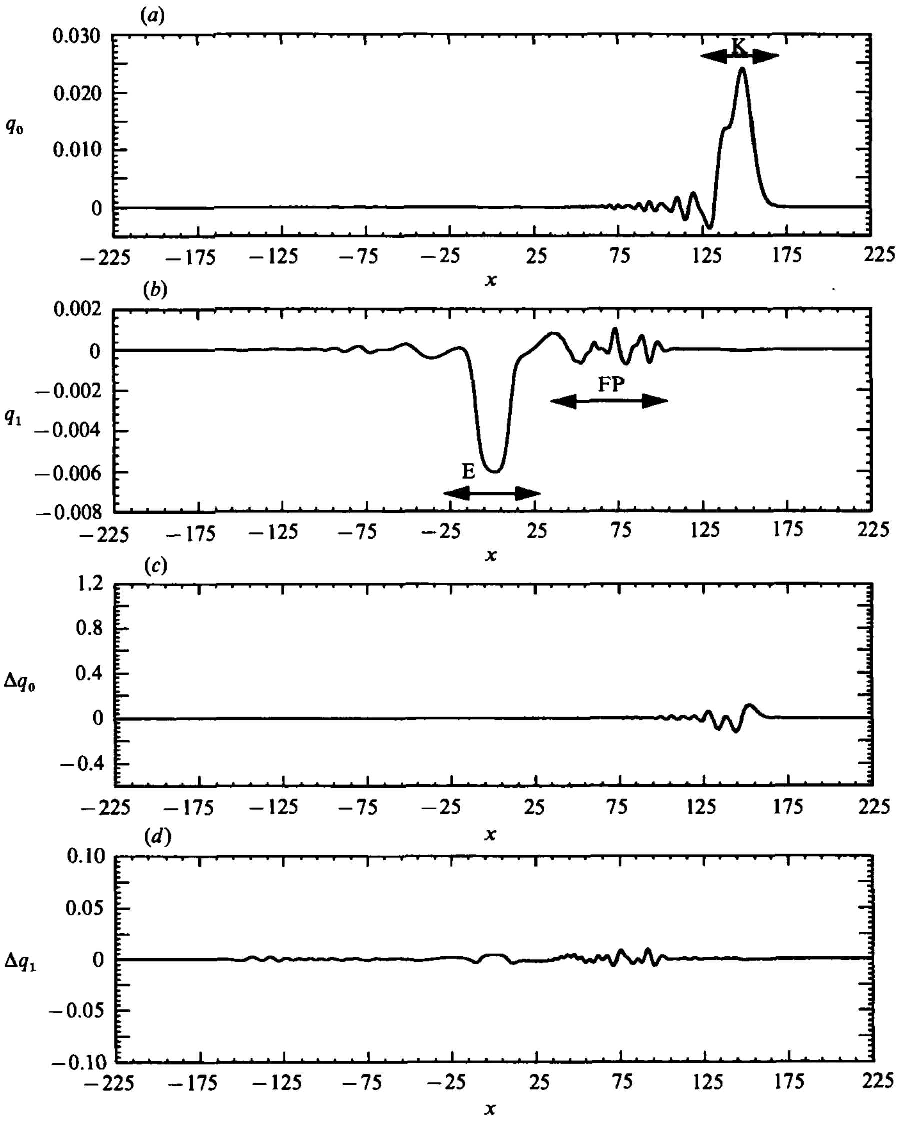

FIGURE 18. As in figure 16, except $\Pi = 0.006$ (Run III).

be used to describe arbitrary transverse variations. Comparing the solution for the Kelvin mode and the Poincaré modes gives a measure of the separation of the two. To quantify the effects of nonlinearity, the linear solution for each mode is subtracted from the corresponding nonlinear one and the difference scaled by the maximum initial amplitude of the mode in question.

We present results from six runs with $\Pi$ ranging from 0.006 to 16. The relevant parameters of the runs are listed in table 1. In figures 16–21 we show plots of the results for all six runs. For each run we have plotted the solutions for the Kelvin and first Poincaré mode of $q$ at $t = 150$ (showing the rotational separation), and the scaled difference between the nonlinear and linear solutions for the same two modes (showing the strength of the nonlinear effects). It proved enough to compare the Kelvin mode of $q$ to the Poincaré modes of $q$, as the Poincaré modes of $r$ are not significant in the leading disturbance moving to the right. Also, recall from §4.1, that

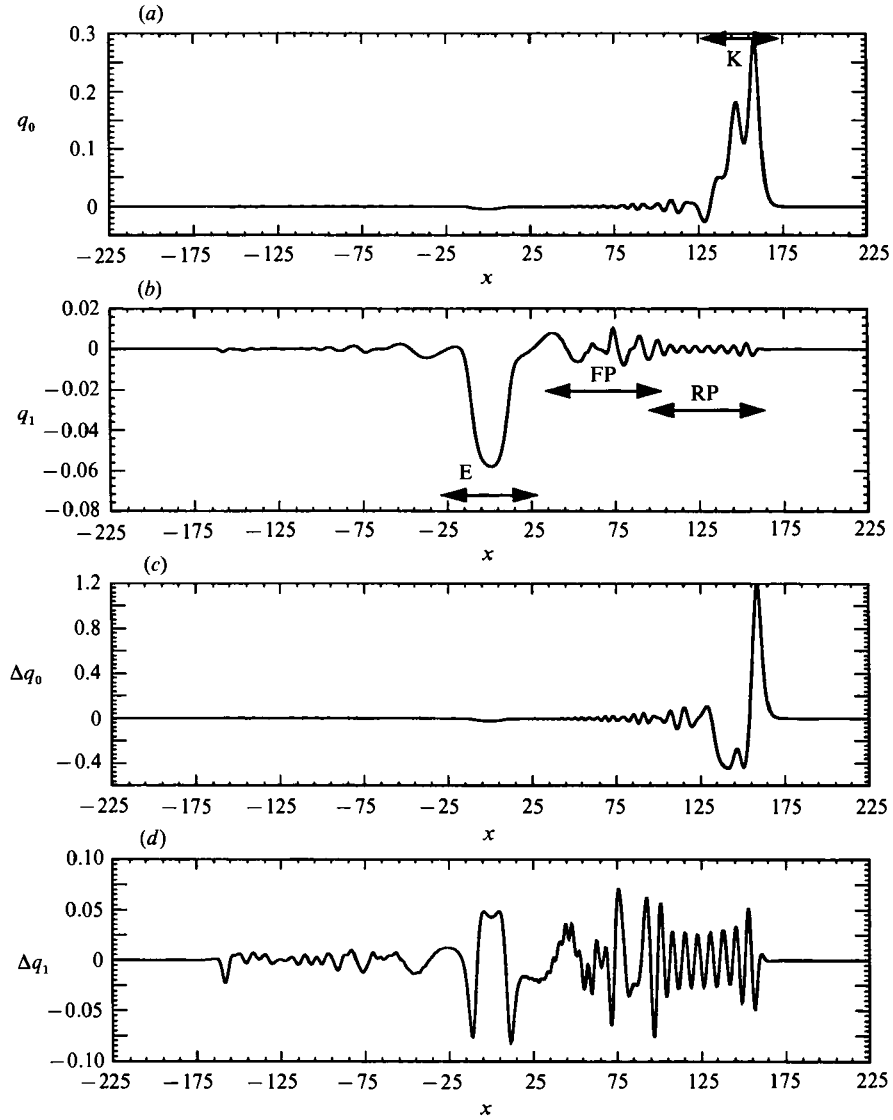

FIGURE 19. As in figure 16, except $\Pi = 0.06$ (Run IV).

for these initial conditions, the disturbances moving to the left and right are basically identical. Note that runs I and II have exactly the same parameters except for the strength of the nonlinearity, it being ten times stronger for the second run than for the first. The same applies to runs III and IV and runs V and VI. The time chosen for the output ($t = 150$) is of the same order of magnitude as the nonlinear timescale for the runs with stronger nonlinearity (runs II, IV and VI), but consequently much smaller than the corresponding nonlinear timescale for the runs with weaker nonlinearity (runs I, III and V).

Runs I, III and IV all have $\Pi \ll 1$. In runs I and III (figures 16 and 18) nonlinear effects are negligible, whereas the rotational separation is quite clear, with the leading Kelvin wave (K) separated from the trailing free Poincaré waves (FP). In run IV (figure 19) the nonlinear evolution is evident with the difference between the nonlinear and linear solutions being of $O(1)$ for both modes. However, the relatively

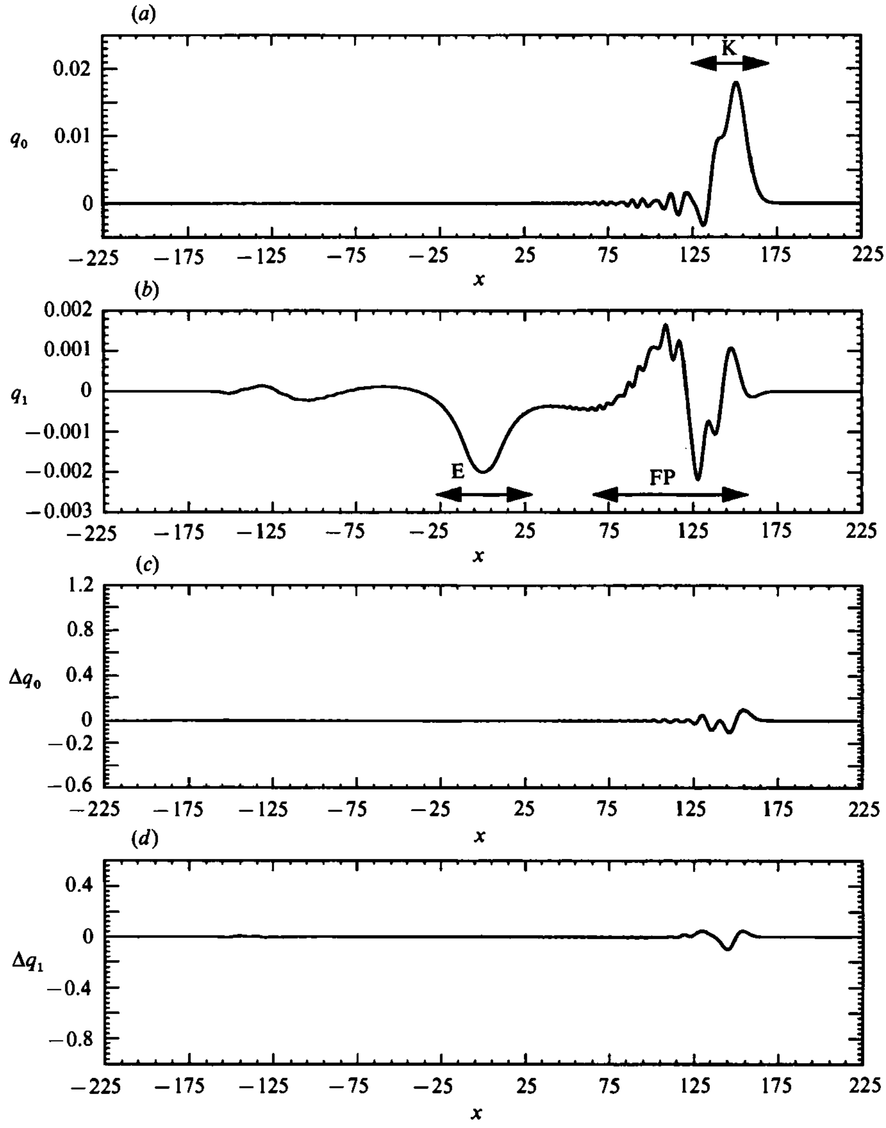

FIGURE 20. As in figure 16, except $\Pi = 1.6$ (Run V).

clear separation of the Poincaré modes of different origin, with the approximately single-frequency leading waves being the resonantly generated Poincaré waves (RP), followed by the transient Poincaré waves (FP), indicates that the rotational separation has taken place before the nonlinear effects become significant, as the magnitude of $\Pi$ indicates. Runs II and V both have $\Pi = O(1)$. In run V (figure 20) neither the rotational separation nor the nonlinear evolution have taken place. On the other hand, in run II (figure 17) these two effects did take place approximately on the same timescale, which is indicated by the Poincaré waves of different origin not being as clearly separable as before. Finally, run VI (figure 21) has $\Pi \gg 1$, with the nonlinear evolution being evident whereas the rotational separation has not taken place and the Poincaré waves of different origin can certainly not be simply separated.

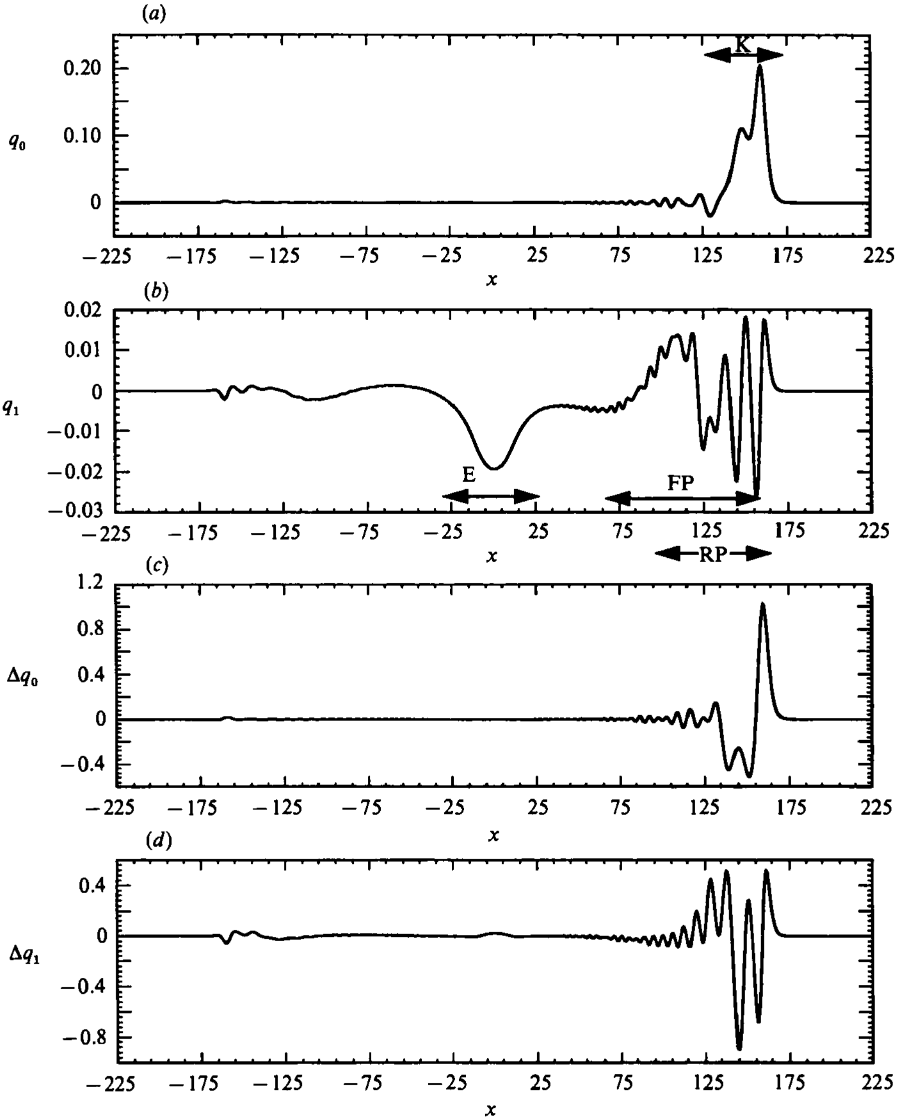

FIGURE 21. As in figure 16, except $\Pi = 16$ (Run VI).

In summary, the above results show the usefulness of the parameter $\Pi$ to predict the importance of nonlinear and rotational effects. For small values of $\Pi$, the rotational separation can be modelled with the linear equations, followed by solving the nonlinear evolution of the leading Kelvin wave disturbance with the coupled evolution equations. In this case, the Poincaré waves of different origin can be clearly separated. For $\Pi \geqslant O(1)$, this separation is not as clear and the full Boussinesq equations have to be employed for the rotational separation.

## 6. Discussion

In this paper we have studied the general problem of geostrophic adjustment in a channel, with weak nonlinear and dispersive effects, which is the appropriate formulation for many internal wave disturbances observed in the oceans and lakes.

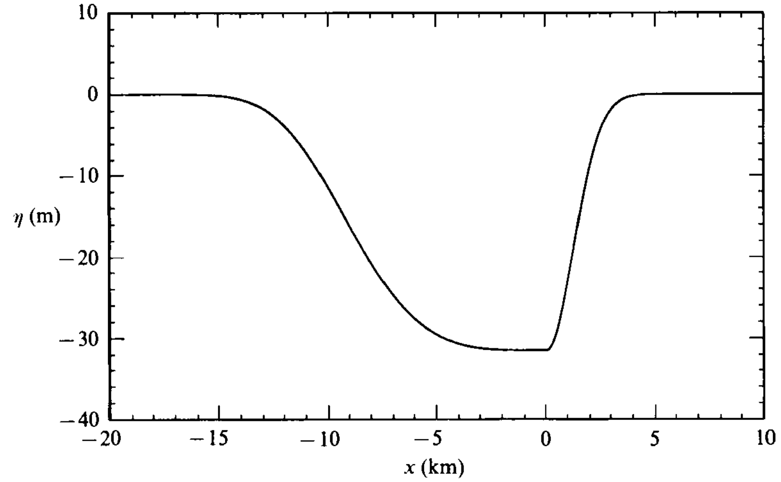

FIGURE 22. The initial disturbance to the interface ($\eta$), used in the computation of nonlinear internal waves in a sea strait.

Our main emphasis has been on the Kelvin and Poincaré waves that evolve from the initial disturbance and their possible interactions, with less attention being paid to the associated advection of the perturbation potential vorticity, which has been studied by Hermann *et al.* (1989). In a separate paper (Renouard *et al.* 1992), numerical solutions based on the Boussinesq equations for a two-layer fluid are compared with experimental measurements. The agreement is very good for moderate nonlinearities, thus confirming the validity of the Boussinesq equations as model equations for this problem.

The two-layer numerical model can be applied to stimulate some of the internal wave motions observed in the field and described in §1. Here we present solutions based on the observations in the Strait of Gibraltar. While the parameters are chosen to match those observed in the natural situation, it should be kept in mind that our formulation is based on certain simplifications, including the assumption of two-layer stratification, a channel of constant width and depth, a simplified initial disturbance, and neglect of tidal currents in the strait. Our purpose here is not to find an exact agreement with incomplete observations, but rather to determine whether the specific features associated with the evolution of nonlinear Kelvin waves in a channel, such as the wavefront curvature due to the nonlinear resonances, are significant in a typical natural situation.

To model the nonlinear internal waves in the Strait, we solve the two-layer Boussinesq equations (Appendix A) with initial conditions similar to those used by Pierini (1989), i.e. a bulge-like depression of the interface, given by

$$\eta(x,y,0)=\begin{cases} a\exp\left[-\left(\dfrac{x-x_0}{X_1}\right)^2\right], & x>0 \\[2ex] a\exp\left[-\left(\dfrac{x-x_0}{X_2}\right)^4\right], & x<0 \end{cases} \tag{6.1}$$

with no transverse variation and no associated flow velocities. The initial disturbance is shown in figure 22. The parameters of the model, listed in table 2, are chosen to be representative of the Strait. Note that the lengthscale of the initial disturbance is

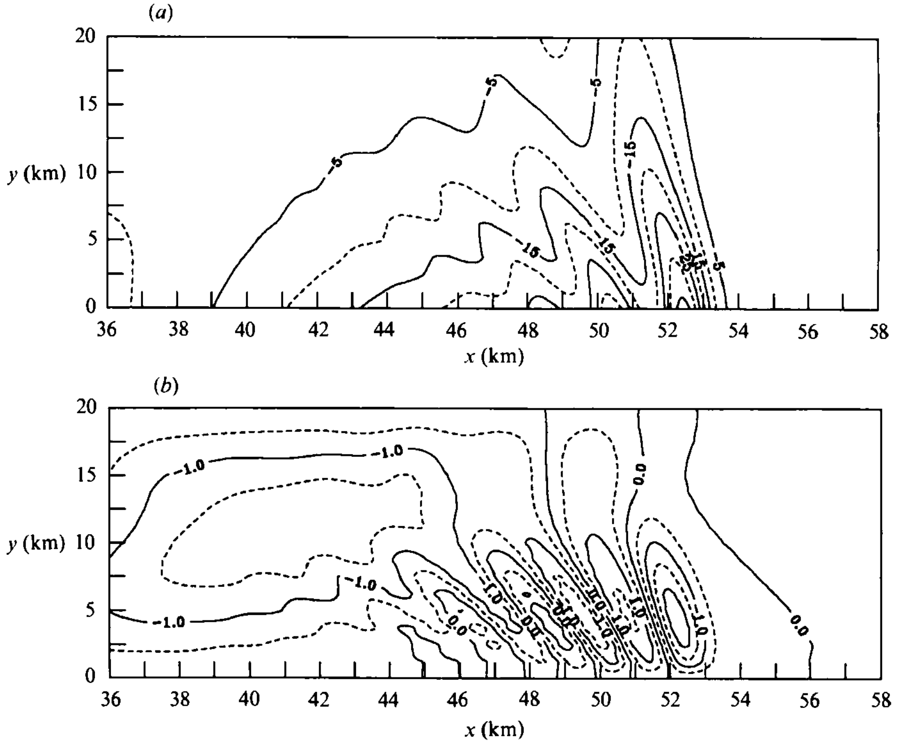

FIGURE 23. Contour plots at $t = 10.9$ hours of the solution for nonlinear internal waves in a sea strait. (*a*) $\eta$ (m). (*b*) $V$ ($m^2/s$).

| | | |
|---|---|---|
| Upper-layer depth | $h_1$ | 150 m |
| Lower-layer depth | $h_2$ | 350 m |
| Linear wave speed | $c_0$ | 1.25 m/s |
| Rossby radius | $R$ | 12.5 km |
| Width of channel | $W$ | 20 km |
| Amplitude of initial disturbance | $a_0$ | 31.5 m |
| Parameter of initial disturbance | $X_1$ | 1.8 km |
| Parameter of initial disturbance | $X_2$ | 10 km |
| Parameter in §5 | $\Pi$ | 1.75 |

TABLE 2. The parameters of the two-layer model used in the computation of nonlinear internal waves in a sea strait

about half that used by Pierini (1989). This shorter disturbance is in accord with Maxworthy (1979), who found the lee wave generated by flow over an obstacle to have a lengthscale comparable to that of the obstacle. We also use smaller amplitudes than Pierini in order to satisfy the assumption of weak nonlinearity.† Note that any effects of the tidal currents in the Strait, which may be important for the periods and lengthscales of the measured waves, are neglected here.

In figure 23 contour plots of the solution for $\eta$ and $V$ (the interface displacement and the transverse horizontal flux in the lower layer) are given at $t = 10.9$ hours. At this time the disturbance has travelled about 50 km, which corresponds approxi-

---

† Pierini (1989) used a larger water depth as his main interest were the waves in the Alboran Sea, which is considerably deeper than the Strait of Gibraltar. Thus, although computing larger wave amplitudes, his nonlinear effects are of comparable strength to those in our computations.

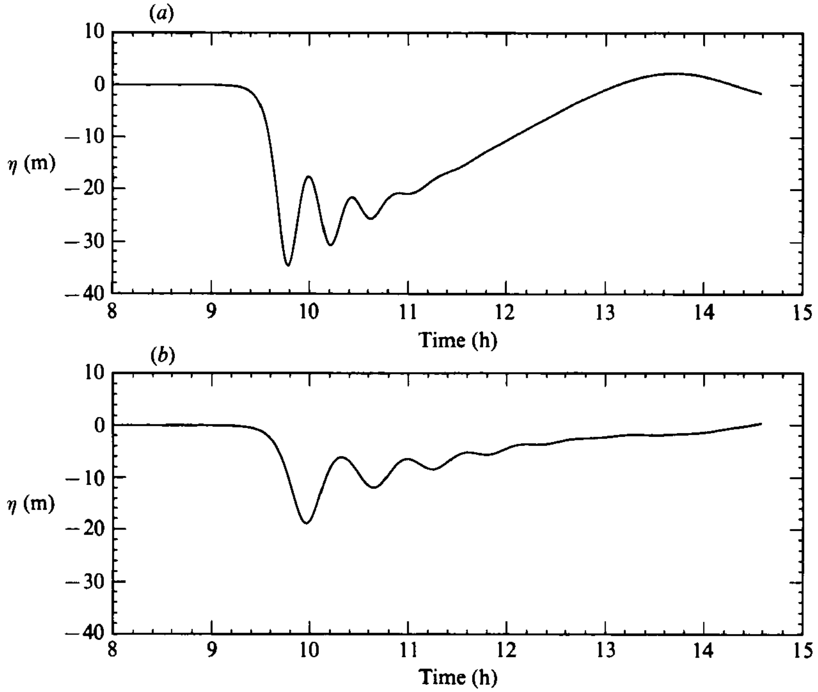

FIGURE 24. Time series of the interface displacement at a distance 46.8 km along a strait from the location of the initial disturbance ($x = 0$) and at two stations across the strait, from the solution for nonlinear internal waves in a sea strait. (a) $y = 0$, (b) $y = \frac{1}{2}W$.

mately to the length of the strait. Figure 24 shows time series of the interface displacement at a distance of 46.8 km along the Strait from the location of the initial disturbance ($x = 0$) and at two stations across the Strait, $y = 0$ and $y = \frac{1}{2}W$.

The computed solutions show a train of nonlinear Kelvin waves evolving from the initial disturbance as it propagates along the strait, in qualitative agreement with the measurements. The transverse Kelvin wave structure and the backward curvature of the wavecrests are clearly visible in the computed solution, with the associated phase shift of the leading wave across the strait being about 700 m. The maximum amplitude of the computed waves of about 35 m at the right-hand coast, which is considerably less than the largest amplitudes observed, is due to our choice of the amplitude of the initial disturbance which was constrained by the assumption of weak nonlinearity in the Boussinesq equations. A typical period of the computed waves is about 30 minutes, corresponding to wavelengths of about 2000 m. This period is considerably larger than the measured one of about 15 minutes. The reason for this discrepancy may be the effect of the strong tidal currents in the strait, which are neglected in the numerical solution, or possibly the smaller amplitudes in the computed solutions, as the timescale of the nonlinear solitary waves decreases with increasing amplitude. A run with initial amplitudes twice as large gave waves with amplitudes at the coast of around 70 m and periods of about 20–25 minutes. However, as noted above, the assumption of weak nonlinear effects is questionable for this run.

It is of interest to consider the effect of friction on the wavefront curvature of the nonlinear Kelvin waves. From linear theory, friction is known to tilt the crests of periodic Kelvin waves backward away from the normal to the coast (Martinsen & Weber 1981). Several authors, among them Grimshaw (1985) and Renouard *et al.*

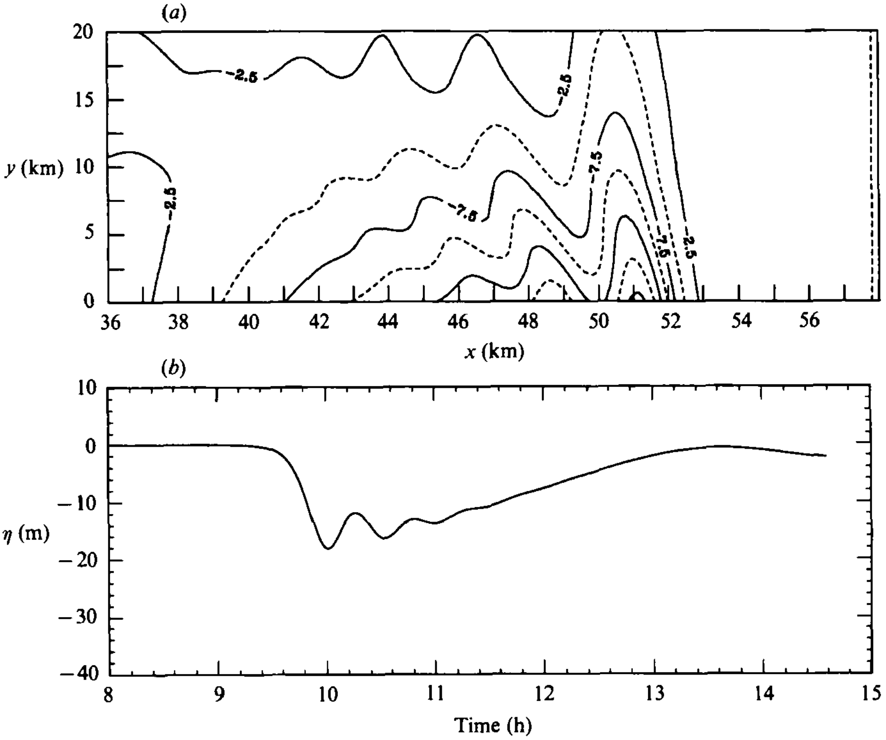

FIGURE 25. The solution for internal waves in a sea strait with frictional effects. (*a*) A contour plot of the solution for $\eta$ (m) at $t = 10.9$ hours (compare to figure 23*a*). (*b*) Timeseries of $\eta$ at 46.8 km along the strait and at $y = 0$ (compare to figure 24*a*).

(1987), have suggested that this might, at least partly, explain the observed backward curvature of nonlinear Kelvin waves. To study this, we repeated the above run with simple linear friction terms included in the two-layer Boussinesq equations (see Appendix A). The strength of the friction was chosen to given an e-folding time of about 18 hours, which is consistent with the measurements of Wesson & Gregg (1988), who estimated the lifetime of a typical wave packet in the Strait to be around 1 day. In figure 25 we show a contour plot of the solution for $\eta$ at $t = 10.9$ hours and a time series of $\eta$ at 46.8 km along the channel and at $y = 0$. These figures correspond to figures 23(*a*) and 24(*a*) for the solution without friction. In both figures we see a considerable attenuation of the wave amplitude with time, due to frictional losses. (These effects may be overestimated due to the neglect of currents in the Strait, as these waves tend to ride with the current along the Strait and thus take less time to propagate along its length.) However, rather than seeing an increased curvature due to frictional effects, as may be expected from linear theory, the curvature is considerably less than that without frictional effects, with the phase shift of the leading wave across the Strait about 350 m, compared to 700 m in the solution without frictional effects. This difference is due to weaker nonlinear resonant effects as the amplitude of the leading wave is smaller. Otherwise, no direct effects of friction on the curvature of the waves or the decay rate across the channel are visible.

This work was supported by the Office of Naval Research (Coastal Sciences). Some of the calculations in this paper were performed on the MIT Supercomputer Facility CRAY-2.

## Appendix A. Derivation of governing equations for a two-layer fluid

We consider the motion of a two-layer fluid confined to a channel rotating on an $f$-plane. For now, the fluid is assumed to be incompressible and inviscid, and frictional effects at the channel walls, bottom and at the interface between the two fluids are neglected. Furthermore, a rigid-lid approximation is made, neglecting the barotropic surface wave mode and looking only at the evolution of the baroclinic internal wave mode. Again, the $x$-axis is taken to be along the channel, the $y$-axis across the channel and the $z$-axis in the vertical direction, positive upwards. The fluid layers have constant densities $\rho_1$ and $\rho_2$ and depths $h_1$ and $h_2$, with the interface between the fluid layers at the equilibrium position $z=0$. Following a derivation exactly like that given in §2 for the corresponding single-layer case (the details of both derivations are given by Tomasson 1991), we get the Boussinesq momentum equations for the upper layer

$$U_t^{(1)}+\alpha U^{(1)}U_x^{(1)}+\alpha\gamma V^{(1)}U_y^{(1)}-\epsilon V^{(1)}+\frac{1}{\rho_1}\bar{p}_x^{(2)}-\frac{1}{\rho_1}\eta_x-\tfrac{1}{3}\beta h_1^2\,(U_{xxt}^{(1)}+\gamma U_{yyt}^{(1)})=O(\beta^2), \tag{A 1}$$

$$\gamma V_t^{(1)}+\alpha\gamma U^{(1)}V_x^{(1)}+\alpha\gamma^2 V^{(1)}V_y^{(1)}+\epsilon U^{(1)}+\frac{\gamma}{\rho_1}\bar{p}_y^{(2)}-\frac{\gamma}{\rho_1}\eta_y-\tfrac{1}{3}\beta\gamma h_1^2\,(V_{xxt}^{(1)}+\gamma V_{yyt}^{(1)})=O(\beta^2), \tag{A 2}$$

and those for the lower layer

$$U_t^{(2)}+\alpha U^{(2)}U_x^{(2)}+\alpha\gamma V^{(2)}U_y^{(2)}-\epsilon V^{(2)}+\frac{1}{\rho_2}\bar{p}_x^{(1)}+\frac{1}{\rho_2}\eta_x-\tfrac{1}{3}\beta h_2^2(U_{xxt}^{(2)}+\gamma U_{yyt}^{(2)})=O(\beta^2), \tag{A 3}$$

$$\gamma V_t^{(2)}+\alpha\gamma U^{(2)}V_x^{(2)}+\alpha\gamma^2 V^{(2)}V_y^{(2)}+\epsilon U^{(2)}+\frac{\gamma}{\rho_2}\bar{p}_y^{(1)}+\frac{\gamma}{\rho_2}\eta_y-\tfrac{1}{3}\beta\gamma h_2^2(V_{xxt}^{(2)}+\gamma V_{yyt}^{(2)})=O(\beta^2), \tag{A 4}$$

together with the continuity equation for the upper layer

$$-\eta_t+[(h_1-\alpha\eta)\,U^{(1)}]_x+\gamma[(h_1-\alpha\eta)\,V^{(1)}]_y=O(\beta^2), \tag{A 5}$$

and that for the lower layer

$$\eta_t+[(h_2+\alpha\eta)\,U^{(2)}]_x+\gamma[(h_2+\alpha\eta)\,V^{(2)}]_y=O(\beta^2). \tag{A 6}$$

Here, $U^{(1,2)}$ and $V^{(1,2)}$ are the depth-averaged horizontal velocities in each layer, $\eta$ is the interface displacement, and $\bar{p}^{(1,2)}$ are the dynamic pressures at the interface, i.e.

$$\bar{p}^{(1,2)}(x,y,t)=p^{(1,2)}\,|_{z=\alpha\eta}, \tag{A 7}$$

where $p$ is the dynamic pressure in the fluid, i.e. the fluid pressure after subtracting the hydrostatic pressure. The scaling used here is

$$\left.\begin{aligned}&x'=k^{-1}x,\quad y'=l^{-1}y,\quad z'=h_0 z,\quad U'^{(1,2)}=\alpha c_0\,U^{(1,2)},\quad V'^{(1,2)}=\alpha\gamma^{\frac{1}{2}}c_0\,V^{(1,2)},\\&t'=\frac{1}{kc_0}t,\quad \eta'=\alpha h_0\,\eta,\quad p'=\alpha\rho_0\,c_0^2\,p,\quad h'_{1,2}=h_0\,h_{1,2},\quad \rho'_{(1,2)}=\rho_0\,\rho_{1,2},\end{aligned}\right\} \tag{A 8}$$

where primes denote the dimensional variables. Here, $h_0=h'_1\,h'_2/(h'_1+h'_2)$ is an equivalent single-layer depth for the corresponding linear and hydrostatic problem, $c_0^2=(\Delta\rho/\rho_0)\,gh_0$ is the linear phase speed of the internal waves, $\Delta\rho=\rho'_2-\rho'_1$ is the density difference and $\rho_0$ is a reference density. The parameters we have introduced are

$$\alpha = a/h_0, \tag{A 9}$$

$$\beta = (kh_0)^2, \tag{A 10}$$

$$\epsilon = \frac{1}{kR}(l/k), \tag{A 11}$$

$$\gamma = (l/k)^2, \tag{A 12}$$

representing nonlinear, dispersive, rotational and transverse effects, respectively. The parameter $a$ is a measure of the amplitude of the disturbance, $k^{-1}$ and $l^{-1}$ are typical lengthscales in the $x$- and $y$-directions, respectively, and $R = c_0/f$ is the internal Rossby radius of deformation. The above equations are based on the assumption of weak nonlinear, dispersive and rotational effects, i.e.

$$\alpha = O(\beta) = O(\epsilon) \ll 1. \tag{A 13}$$

To obtain one pair of momentum equations we take the difference between the momentum equations in the two layers, i.e. $\rho_2 \times$ (A 3) $- \rho_1 \times$ (A 1) and $\rho_2 \times$ (A 4) $- \rho_1 \times$ (A 2). Assuming

$$\Delta\rho/\rho_0 \ll O(\beta), \tag{A 14}$$

which is an appropriate assumption for the cases considered here, and requiring that the mass fluxes in the two layers balance in the $x$- and $y$-directions independently, i.e.

$$(h_1-\alpha\eta)\,(U^{(1)}, V^{(1)}) = -(h_2+\alpha\eta)\,(U^{(2)}, V^{(2)}), \tag{A 15}$$

which is the case for the lowest-order linear and hydrostatic problem, we get after using the appropriate matching conditions at the interface between the two layers, the following set of Boussinesq equations:

$$\eta_t+U_x+\gamma V_y = O(\beta^2), \tag{A 16}$$

$$U_t+\eta_x-\epsilon V+\alpha\left[\frac{1}{h_2}-\frac{1}{h_1}\right](2UU_x+\gamma(VU)_y-\eta U_t)-\tfrac{1}{3}\beta h_1 h_2(U_{xxt}+\gamma U_{yyt}) = O(\beta^2), \tag{A 17}$$

$$\gamma V_t+\gamma\eta_y+\epsilon U+\alpha\gamma\left[\frac{1}{h_2}-\frac{1}{h_1}\right]((UV)_x+2\gamma VV_y-\eta V_t)-\tfrac{1}{3}\beta\gamma h_1 h_2(V_{xxt}+\gamma V_{yyt}) = O(\beta^2), \tag{A 18}$$

with the sidewall boundary conditions,

$$V = 0 \quad \text{at} \quad y = 0, W. \tag{A 19}$$

Here, $\eta$ is the interface displacement and $U$ and $V$ are the horizontal fluxes in the lower layer

$$(U, V) = (h_2+\alpha\eta)\,(U^{(2)}, V^{(2)}), \tag{A 20}$$

or equivalently, from (A 15), the negative fluxes in the upper layer. Equation (A 16) represents the continuity equation for either layer, whereas (A 17) and (A 18) come from the difference between the momentum equations in the two layers. We have also assumed that

$$\left[\frac{1}{h_2}-\frac{1}{h_1}\right] = O(1), \tag{A 21}$$

which is generally true for the cases considered here.

For the solutions with frictional effects presented in §6, we include simple linear friction terms (see for example Martinsen & Weber 1981) to represent the friction at the bottom and at the interface between the fluid layers. This gives the equations

$$\eta_t + U_x + \gamma V_y = O(\beta^2), \qquad \text{(A 22)}$$

$$U_t + \eta_x - \epsilon V + \alpha\left[\frac{1}{h_2} - \frac{1}{h_1}\right](2UU_x + \gamma(VU)_y - \eta U_t) - \tfrac{1}{3}\beta h_1 h_2(U_{xxt} + \gamma U_{yyt}) + \lambda U = O(\beta^2), \qquad \text{(A 23)}$$

$$\begin{aligned}\gamma V_t + \gamma\eta_y + \epsilon U + \alpha\gamma\left[\frac{1}{h_2} - \frac{1}{h_1}\right]((UV)_x + 2\gamma VV_y - \eta V_t) - \tfrac{1}{3}\beta\gamma h_1 h_2(V_{xxt} + \gamma V_{yyt}) + \gamma\lambda V \\ = O(\beta^2), \qquad \text{(A 24)}\end{aligned}$$

where

$$\lambda = (1/kc_0)K, \qquad \text{(A 25)}$$

and $K$ is the dimensional friction coefficient.

## Appendix B. Numerical scheme

The Boussinesq equations (3.1)–(3.3) are solved numerically using a line-by-line iteration scheme developed and described in detail by Pedersen & Rygg (1987), Pedersen (1988) and Rygg (1988). They developed the scheme for the equations without rotation, but we have extended it to include the rotational terms. To assist in presenting the scheme, we define a difference operator in the $x$-direction

$$\delta_x F^n_{p,q} = \frac{1}{\Delta x}(F^n_{p+\frac{1}{2},q} - F^n_{p-\frac{1}{2},q}), \qquad \text{(B 1)}$$

and an average operator in the $x$-direction

$$(\overline{F}^x)^n_{p,q} = \tfrac{1}{2}(F^n_{p+\frac{1}{2},q} + F^n_{p-\frac{1}{2},q}), \qquad \text{(B 2)}$$

with corresponding operators defined for the $y$-direction and time, $t$. Here, $F^n_{p,q}$ is the discrete approximation to a quantity $F$ at the gridpoint with coordinates ($p\,\Delta x$, $q\,\Delta y$, $n\,\Delta t$), where $\Delta x$, $\Delta y$ and $\Delta t$ are the space and time increments, respectively. The space and time discretizations are done on a staggered grid. In the discrete coordinates, the variables to be solved for are

$$\eta^n_{p+\frac{1}{2},q+\frac{1}{2}}, \quad U^{n+\frac{1}{2}}_{p,q+\frac{1}{2}}, \quad V^{n+\frac{1}{2}}_{p+\frac{1}{2},q}, \quad \dot{U}^n_{p,q+\frac{1}{2}}, \quad \dot{V}^n_{p+\frac{1}{2},q}, \qquad \text{(B 3)}$$

where $U$ and $V$ are the horizontal fluid accelerations.

The scheme consists of three separate steps: a predictor–corrector step to solve for the surface displacement ($\eta$) from a discrete version of the continuity equation (3.1),

$$[\delta_t\,\eta + \delta_x\{(1+\overline{\eta}^x)\,U\} + \Gamma\delta_x\{(1+\overline{\eta}^y)V\}]^{n+\frac{1}{2}}_{p+\frac{1}{2},q+\frac{1}{2}} = 0; \qquad \text{(B 4)}$$

an alternating direction implicit (ADI) iteration scheme to solve for the fluid accelerations ($\dot{U}$ and $\dot{V}$) from discrete versions of the momentum equations (3.2) and (3.3),

$$\begin{aligned}&[\dot{U} + \delta_x\,\eta + \tfrac{1}{2}\delta_x((\overline{U^{n-\frac{1}{2}}}^{x})^2 + \Delta t\,\overline{U^{n-\frac{1}{2}}}^{x}\,\overline{(\dot{U})}^{x}) \\ &\qquad + \Gamma[\overline{V^{n-\frac{1}{2}}}^{xy} + \tfrac{1}{2}\Delta t\,\overline{(\dot{V})}^{xy})\,\delta_y(\overline{U^{n-\frac{1}{2}}}^{y} + \tfrac{1}{2}\Delta t\,\overline{(\dot{U})}^{y}) \\ &\qquad\qquad - \Gamma[\overline{V^{n-\frac{1}{2}}}^{xy} + \tfrac{1}{2}\Delta t\,\overline{(\dot{V})}^{xy}) - \tfrac{1}{3}(\delta_x^2\dot{U} + \Gamma\delta_y^2\dot{U})]^n_{p,q+\frac{1}{2}} = 0, \qquad \text{(B 5)}\end{aligned}$$

$$\begin{aligned}&[\dot{V} + \delta_y\,\eta + (\overline{U^{n-\frac{1}{2}}}^{xy} + \tfrac{1}{2}\Delta t\,\overline{(\dot{U})}^{xy})\,\delta_x(\overline{V^{n-\frac{1}{2}}}^{x} + \tfrac{1}{2}\Delta t\,\overline{(\dot{V})}^{x}) \\ &\qquad + \frac{\Gamma}{2}\delta_y((\overline{V^{n-\frac{1}{2}}}^{y})^2 + \Delta t\,\overline{V^{n-\frac{1}{2}}}^{y}\,\overline{(\dot{V})}^{y}) \\ &\qquad\qquad + (\overline{U^{n-\frac{1}{2}}}^{xy} + \tfrac{1}{2}\Delta t\,\overline{(\dot{U})}^{xy}) - \tfrac{1}{3}(\delta_x^2\dot{V} + \Gamma\delta_y^2\dot{V})]^n_{p+\frac{1}{2},q} = 0, \qquad \text{(B 6)}\end{aligned}$$

where the double overbars indicate averaging in both $x$ and $y$, and a simple timestepping by a midpoint rule to solve for the velocities ($U$ and $V$) from discrete versions of the kinematic conditions:

$$[\delta_t U - \dot{U}]^n_{p,q+\frac{1}{2}} = 0, \tag{B 7}$$

$$[\delta_t V - \dot{V}]^n_{p+\frac{1}{2},q} = 0. \tag{B 8}$$

The typical number of iterations needed in the ADI scheme were between two and four with typical gridspacings and timestep of $\Delta x = 0.15$, $\Delta y = 0.1$ and $\Delta t = 0.1$.

## Appendix C. The timescale of rotational separation

The linear dispersion relationship for the Kelvin mode of the Boussinesq equations, (2.23)–(2.25), is

$$\omega^2 = \kappa^2, \tag{C 1}$$

and for the Poincaré modes

$$\omega^2 = \kappa^2 + \epsilon[1+(n\pi/W)^2], \quad n = 1,2,\ldots \tag{C 2}$$

The dispersive effects are not of importance for this analysis, thus we have set $\beta = 0$. We have also taken the lengthscale in the $y$-direction to the Rossby radius, thus

$$\gamma = \epsilon = (kR)^{-2}. \tag{C 3}$$

Otherwise, the scaling is that given by (2.4). In this scaling, distances in the $x$-direction are scaled by a typical wavelength and time is scaled by a typical wave period; thus $\omega$ and $\kappa$ are $O(1)$. From the dispersion relationships we get the group speed of the Kelvin wave moving to the right:

$$c_g|_x = \partial\omega/\partial\kappa = 1, \tag{C 4}$$

and the group speed of the Poincaré modes moving to the right:

$$c_g|_x = \frac{\partial\omega}{\partial\kappa} = \frac{\kappa}{\{\kappa^2+\epsilon[1+(n\pi/W)^2]\}^{\frac{1}{2}}}, \quad n = 1,2,\ldots \tag{C 5}$$

The difference in the group speed is

$$\Delta c_g|_x = 1 - \frac{\kappa}{\{\kappa^2+\epsilon[1+(n\pi/W)^2]\}^{\frac{1}{2}}} = \tfrac{1}{2}\epsilon\frac{1+(n\pi/W)^2}{\kappa^2} + O(\epsilon^2), \tag{C 6}$$

where we have used the assumption of weak rotational effects, i.e. $\epsilon \ll 1$. Assuming that the width of the channel is of the order of a Rossby radius, i.e. $O(1)$ in this scaling, we get the time for the waves to separate one wavelength in space

$$T_R = O(\epsilon^{-1}) = O(kR)^2. \tag{C 7}$$

Note that this analysis also holds for $\epsilon = O(1)$, as the difference in group speed is then $\Delta c_g|_x = O(1)$ and consequently $T_R = O(1)$.

## REFERENCES

Armi, L. & Farmer, D. M. 1988 The flow of Mediterranean water through the Strait of Gibraltar. *Prog. Oceanogr.* **21**, 1–105.

Farmer, D. M. 1978 Observations of long nonlinear internal waves in a lake. *J. Phys. Oceanogr.* **8**, 63–73.

FARMER, D. M. & ARMI, L. 1988 The flow of Atlantic water through the Strait of Gibraltar. *Prog. Oceanogr.* **21**, 1–105.

FARMER, D. M. & SMITH, J. D. 1988 Nonlinear internal waves in a fjord. In *Hydrodynamics of Estuaries and Fjords*. Elsevier.

GARGETT, A. E. 1976 Generation of internal waves in the Strait of Georgia, British Columbia. *Deep-Sea Res.* **23**, 17–32.

GILL, A. E. 1976 Adjustment under gravity in a rotating channel. *J. Fluid Mech.* **77**, 603–621.

GILL, A. E. 1982 *Atmosphere–Ocean Dynamics*. Academic.

GRIMSHAW, R. 1985 Evolution equations for weakly nonlinear, long internal waves in a rotating fluid. *Stud. Appl. Maths* **73**, 1–33.

GRIMSHAW, R. & MELVILLE, W. K. 1989 On the derivation of the modified Kadomtsev–Petviashvili equation. *Stud. Appl. Maths* **80**, 183–202.

HAMMACK, J. L. & SEGUR, H. 1978 Modelling criteria for long water waves. *J. Fluid Mech.* **84**, 359–373.

HERMANN, A. J., RHINES, P. B. & JOHNSON, E. R. 1989 Nonlinear Rossby adjustment in a channel: beyond Kelvin waves. *J. Fluid Mech.* **205**, 469–502.

HUNKINS, K. & FLIEGEL, M. 1973 Internal undular surges in Seneca Lake: A natural occurrence of solitons. *J. Geophys. Res.* **78**, 539–548.

KATSIS, C. & AKYLAS, T. R. 1987 Solitary internal waves in a rotating channel: A numerical study. *Phys. Fluids* **30**, 297–301.

LACOMBE, H. & RICHEZ, C. 1982 The regime of the Straits of Gibraltar. In *Hydrodynamics of Semi-Enclosed Seas* (ed. J. C. J. Nihoul), pp. 13–73. Elsevier.

LA VIOLETTE, P. E. & ARNONE, R. A. 1988 A tide-generated internal waveform in the western approaches to the Strait of Gibraltar. *J. Geophys. Res.* **93**, 15653–15667.

MARTINSEN, E. A. & WEBER, J. E. 1981 Frictional influence on internal Kelvin waves. *Tellus* **33**, 402–410.

MAXWORTHY, T. 1979 A note on the internal solitary waves produced by tidal flow over a three-dimensional ridge. *J. Geophys. Res.* **84**, 338–346.

MAXWORTHY, T. 1983 Experiments on solitary internal Kelvin waves. *J. Fluid Mech.* **129**, 365–383.

MELVILLE, W. K., TOMASSON, G. G. & RENOUARD, D. P. 1989 On the stability of Kelvin waves. *J. Fluid Mech.* **206**, 1–23.

PEDERSEN, G. 1988 On the numerical solution of the Boussinesq equations. *Res. Rep.* University of Oslo, Department of Mathematics.

PEDERSEN, G. & RYGG, O. B. 1987 Numerical solution of the three dimensional Boussinesq equations for dispersive surface waves. *Res. Rep.* 1. University of Oslo, Institute of Mathematics.

PIERINI, S. 1989 A model for the Alboran Sea internal solitary waves. *J. Phys. Oceanogr.* **19**, 755–772.

RENOUARD, D. P., CHABERT D'HIERES, G. & ZHANG, X. 1987 An experimental study of strongly nonlinear waves in a rotating system. *J. Fluid Mech.* **177**, 381–394.

RENOUARD, D. P., TOMASSON, G. G. & MELVILLE, W. K. 1992 An experimental and numerical study of nonlinear internal waves.

RYGG, O. B. 1988 Nonlinear refraction-diffraction of surface waves in intermediate and shallow water, *Coastal Engng.* **12**, 191–211.

THORPE, S. A., HALL, A. & CROFTS, I. 1972 The internal surge in Loch Ness. *Nature* **237**, 96–98.

TOMASSON, G. G. 1991 Nonlinear waves in a channel: Three-dimensional and rotational effects. Doctoral Thesis, Department of Civil Engineering, Massachusetts Institute of Technology.

TOMASSON, G. G. & MELVILLE, W. K. 1990 Nonlinear and dispersive effects in Kelvin waves. *Phys. Fluids* A **2**, 189–193.

WESSON, J. C. & GREGG, M. C. 1988 Turbulent dissipation in the Strait of Gibraltar and associated mixing. In *Small-scale Turbulence and Mixing in the Ocean: Proc. 19th Intl. Liège Coll. on Ocean Hydrodyn* (ed. J. C. J. Nihoul & B. M. Jamart), pp. 201–212. Elsevier.

ZIEGENBEIN, J. 1969 Short internal waves in the Strait of Gibraltar. *Deep-Sea Res.* **16**, 479–487.